Influence of exchange bias on magnetic losses in CoFeB/MgO/CoFeB tunnel junctions

Ryan Stearrett, W. G. Wang, Xiaoming Kou, J. F. Feng, J. M. D. Coey, J. Q. Xiao, and E. R. Nowak

Phys. Rev. B **86**, 014415 — Published 16 July 2012

DOI: 10.1103/PhysRevB.86.014415

Influence of exchange bias on magnetic losses in CoFeB/MgO/CoFeB tunnel junctions

Ryan Stearrett[1], W. G. Wang[1], Xiaoming Kou[1], J. F. Feng[2], J. M. D. Coey[2], J. Q. Xiao[1], and E. R. Nowak[1]

[1]Department of Physics and Astronomy, University of Delaware, Newark, DE 19716, USA
[2]CRANN and School of Physics, Trinity College, Dublin 2, Ireland

Abstract

The strength of the exchange bias field is found to influence the low-frequency magnetoresistive noise associated with the magnetic reference layer in sputtered-deposited and electron-beam evaporated CoFeB/MgO/CoFeB tunnel junctions. The noise is due to magnetic losses arising in the reference layer. The losses are parameterized by a phase lag ε which exhibits a non-trivial dependence on the externally applied field. The general trend found amongst all devices is that the losses are largest in the antiparallel state. The effect of exchange bias on the reference's layers noise is investigated at a field corresponding to maximum resistance susceptibility, H_{ref}. Higher values for the phase lag at H_{ref}, ε_{ref}, are found in devices having a large exchange bias field. We also observed that H_{ref} and ε_{ref} are larger in devices having thicker seed layers. This characteristic is also evident in double-barrier magnetic tunnel junctions. Prolonged thermal annealing is found to decrease ε_{ref}, reduce H_{ref}, and alter the field profile of the resistance susceptibility of the reference layer to resemble that of a more magnetically soft behavior. In addition to its impact on the magnetoresistive noise, the incorporation of exchange bias layers into the materials stack also affects the tunneling magnetoresistance ratio with higher values found at smaller exchange bias fields. We attribute the magnitude of the magnetic losses, and hence the magnetoresistive noise, from the reference layer to disorder in its magnetic microstructure. Our results indicate that the nature and degree

of disorder are correlated to the strength of the exchange bias coupling. The origin of this correlation may be due to a competition between different microstructures among various layers; one that leads to coherent tunneling (large tunneling magnetoresistance) in MgO-based tunneling devices and the other which promotes strong exchange bias coupling. A decrease in the exchange bias either through degradation from thermal treatments or by varying the thickness of the underlying seed layer will lead to less magnetic disorder in the system. We show that the magnetoresistive noise can be used to probe magnetic disorder in exchange-biased devices through the determination of the magnetic losses.

I. INTRODUCTION

The contact of a ferromagnetic (FM) with an antiferromagnetic (AF) material will give rise to a preferred relative orientation of the moments of the two different magnetic materials, called exchange coupling. Consequently, there is a displacement of the hysteresis loop of the FM material along its field axis. In 1956, Meiklejohn and Bean[1] discovered a unique unidirectional anisotropy, which is known as exchange anisotropy, in Co nanoparticles with a thin layer of CoO on the surface. Exchange bias occurs when the Curie temperature of the FM is greater than the Néel temperature, T_N, of the AF. When the temperature drops below T_N in the presence of an external field sufficient to saturate the FM, the magnetic moments of the AF material minimize their interaction energy with the FM material by selecting a preferred magnetization direction. As long as the FM/AF system is not heated above T_N, the FM material will be biased in the same direction as it had at T_N.

Exchange bias is considered an essential component for spintronics devices. Giant magnetoresistance (GMR) is observed when electrons travel through a magnetic structure consisting of two FM layers separated by a non-magnetic (NM) metal layer. GMR is attributed to spin-dependent scattering,[2,3] and is reliant on the relative orientation of the FM electrodes.[4] Grünberg *et al*.[5] discovered AF exchange coupling of the Fe layers in the Fe/Cr/Fe system. Without exchange bias, the study of GMR was limited to systems with AF coupling between adjacent FM layers in superlattices[6] or with different coercivities due to different thicknesses of the uncoupled FM layers.[7] However, in all cases the strength of AF coupling is too large for practical applications, which requires low fields to switch from low to high resistance. GMR spin-valves (SVs) are fabricated to provide magnetic pinning through the contact of an AF layer to one FM layer.[8] This creates a well-defined antiparallel (AP) state for a certain range of fields.

With exchange bias, the magnetoresistance changes in fields of a few milliteslas rather than teslas so that a small field is sufficient to alter the angle between the moments of the two FM layers.

The GMR SV is a simple structure that illustrates the basic role of exchange bias in spintronic devices but more complicated structures, such as the magnetic tunnel junction (MTJ), offer larger signals. A celebrated example of a MTJ is one that incorporates a MgO tunnel barrier. Through thermal annealing, the MgO barrier imposes its (001) crystal structure onto the adjacent CoFeB layers which results in coherent tunneling of electrons and high tunneling magnetoresistance (TMR).[9] TMR is due to spin-dependent electron tunneling. The largest experimental value of 604 % was observed in a pseudo-SV MTJ,[10] but this value is still well below the theoretical prediction of 34000 % using FeCo(100)/MgO(100)/FeCo(100).[11] A pseudo-SV MTJ is not suitable for applications due to a lack of magnetic pinning such that the two FM layers switch at different fields due to different coercivities.

The incorporation of a seed layer, an AF layer, and a synthetic antiferromagnetic (SAF) construction are essential additions to the MTJ for their use as magnetic sensors or in magnetic random access memory. The SAF is an antiferromagnetically-coupled FM/NM/FM trilayer, which is exchange-biased by the AF layer. Lee *et al.*[12] showed that the Ru spacer in the SAF allowed the CoFeB reference layer to form a (001)-oriented bcc structure, which achieved 361 % TMR in exchange-biased MTJs. Without this spacer, the largest TMR was only 181 %. In Fig. 1, we show the magnetization and TMR as a function of the field applied parallel to the exchange bias direction of an exchange-biased MTJ. The two FM layers of interest are the free and reference layers because their magnetization reversals cause the resistance change. When the applied magnetic field is ramped down from the positive direction, the sudden reversal near zero

field is the switching of the free layer from a parallel (P) to an AP state, which causes the resistance to increase. The more gradual reversal near −35 mT is due to the reference layer switching the device from an AP (high resistance) to a P (low resistance) state. Two other FM layers switch at positive fields and will be discussed later.

The degree of (111) texture in the AF layer is a key factor in determining the strength of the exchange bias.[13] It was discovered that highly textured AF layers resulted in larger exchange bias coupling and that the degree of texture was dependent on the seed layer.[14] A highly textured AF was also found to cause a ripple pattern in the magnetic domain structure. These local magnetization fluctuations within the layer can be a source of magnetoresistive (MR) 1/*f* noise.[15] Thermal annealing was found to create smoother domain boundaries with a finer (smaller length scale) magnetic ripple pattern. Evidently, devices with exchange bias coupling induce elevated MR noise levels even after high temperature annealing.

MR noise is but one of a number of noise mechanisms present in MTJs. The distinct noise contributions in MTJs have recently been summarized.[16] It has been shown that the electronic 1/*f* noise arising from the tunnel barrier can be substantially reduced through thermal annealing.[17-19] As a result, the MR 1/*f* noise, which is largest around the magnetization reversals of the free and reference layers, becomes the dominant source at low frequencies.[20-22] Ozbay *et al*.[23] characterized the MR noise in terms of the magnetic losses of the magnetic layers through the fluctuation-dissipation (FD) theorem. Stearrett *et al*.[24] showed that the magnetic losses of the reference layer were diminished after prolonged annealing and attributed the reduction to a smoother magnetic microstructure in exchange-biased MTJs. In addition, annealing was found to narrow the range of fields required to reverse the reference layer so that the field near maximum resistance susceptibility shifted closer to zero field.

Here, we report on how the magnetic losses responsible for the MR $1/f$ noise of the reference layer, ε_{ref}, are directly related to the magnitude of the field, H_{ref}, at which the resistance susceptibility is a maximum. H_{ref} is shown to depend on the seed layer of the device and the thermal annealing treatments to which it is subjected. Thicker seed layers show better coupling, which produces larger values for H_{ref} and ε_{ref}. Thermal annealing reduces the exchange bias, decreases ε_{ref} and H_{ref}, and alters the magnetic field dependence of the resistance susceptibility of the reference layer such that it resembles the characteristic form of a magnetically soft layer. Double-barrier magnetic tunnel junctions (DMTJs), which incorporate both top and bottom pinning configurations for the same annealing treatment, are used to further investigate the relation between thicker seed layer and stronger exchange bias coupling. We also find that a reduction in exchange bias, and hence magnetic disorder, is correlated with increased TMR which we attribute to a competition between the different microstructures in the exchange bias layers and the CoFeB/MgO/CoFeB trilayer. These studies illustrate how magnetoresistive noise can probe magnetic disorder in exchange-biased devices through the determination of the magnetic losses.

II. EXPERIMENTAL METHODS

We report data on 11 devices (S1 through S11) having different material stack structures and different degrees of exchange bias coupling. The material stacks were deposited by dc-magnetron sputtering except for the MgO layers in devices S7 and S8, which were grown by electron-beam evaporation. Figure 2 illustrates the different stack structures between exchange-biased single-barrier MTJs (S1 through S8), DMTJs (S9),[17] and GMR SVs (S10 and S11).[25,26] GMR SVs have the simplest stack structure consisting of Substrate / Buffer / Free / NM metal / Pinned / AF / Capping layers. The stack for MTJs is Substrate / Buffer / Seed / AF / Pinned / Spacer / Reference / Barrier / Free / Capping. DMTJs contain Substrate / Buffer / Seed / AF / Pinned / Spacer / Reference / Barrier / Free / Barrier / Reference / Spacer / Pinned / AF / Capping. The compositions of the individual layers for each of the devices are shown in Table I. Starting from the substrate, a NM metal thin film usually serves as a buffer layer to provide the desirable growth texture in the subsequently deposited layers. The seed layer corresponds to the layer underneath of an AF layer. In all devices studied, the seed layer is FM (CoFe or NiFe). Magnetically soft FM layers are denoted by 'free,' whereas 'reference' indicates the exchange-biased FM layer adjacent to the barrier and 'pinned' signifies the FM layer in contact with the AF. A NM metal spacer layer is used to provide AF coupling between two FM layers. The structure is then 'capped' with one or more metallic layers to prevent oxidation. The contributions of the seed and pinned layers to the magnetics of the device are usually not discernable in the magnetoresistance but can be detected in a magnetization measurement. For example, in Fig. 1, the seed layer switches around 25 mT, but no effect on the TMR is seen; the pinned layer switches beyond 100 mT (not shown).

Devices having either top, bottom, or both top and bottom pinning configurations were studied. In the top pinning configuration, the AF layer is grown on top of the pinned layer whereas for bottom pinning the AF is underneath the pinned layer. GMR SVs are top-pinned, MTJs are bottom-pinned, and DMTJs incorporate both pinning configurations. Even though the stack structures in DMTJs are symmetric about the free layer, the corresponding seed layers for the top and bottom pinning SAFs are different. DMTJs are convenient for investigating how the strength of the exchange bias coupling is dependent on the seed layer, as will be described below.

Devices S1 through S6 were fabricated into circular, 20 μm diameter, tunnel junctions using UV photolithography and ion-beam etching. S8 and S9 were patterned into 5×15 and 20×20 μm^2 junctions. Electron-beam lithography was used to pattern S7 with an area of 6×1.6 μm^2. The bottom and top lead electrodes connecting to the junctions were patterned into a cross-shaped geometry. GMR SVs were patterned into devices having sizes 5×35 μm^2 for S10 and 2×90 μm^2 for S11. Exchange pinning and shape anisotropy were used to achieve a perpendicular magnetic configuration between the free and reference layers of the GMR SVs. All devices were thermally annealed at a fixed temperature and in an inert gas environment. To establish the exchange bias direction, S1 through S6 were cooled naturally in a field of 120 mT, 800 mT for devices S7 through S9, and 20 and 400 mT for S10 and S11, respectively.

Resistance and the voltage noise were measured simultaneously under constant current bias conditions and as a function of external magnetic field, *H*. The magnetic field was applied in plane and collinear with the exchange bias field direction for MTJs but transverse to the long axis for GMR SVs (perpendicular to the magnetic easy axis of the SV free layer). All data were taken at room temperature using four-probe electrical measurements. The low-frequency voltage

fluctuations were amplified, antialias filtered, and digitized using a 16 bit analog-to-digital converter after which the power spectral density $S_V(f)$ was computed as a function of frequency f. Additional experimental details can be found in Ref. 18. Positive voltage biases correspond to electron transport from the bottom to the top electrode for MTJs. The current is injected at the ends of the long axis of the SVs. More information related to S9, S10, and S11 can found in Refs. 17, 25, and 26, respectively.

III. RESULTS

The power spectral density of the MR noise, $S_V^{mag}(f)$, was obtained by subtracting the contributions from the amplifier noise, thermal and shot noise, and electronic 1/*f* noise from the measured voltage noise power spectral density, $S_V(f)$.[16] Artifacts from electrical interference, such as narrow-band spectral spikes, caused by 60 Hz and by its harmonics, were removed. The noise power spectrum was then integrated across an octave centered at a particular frequency. Figure 3 shows examples of the normalized MR noise power (averaged over the octave), fS_V^{mag}/V^2, as a function of (octave) frequency for four different MTJs. Plotted this way, a 1/*f* spectrum corresponds to an octave power that is frequency-independent, as evident in Fig. 3. The second octave is centered at 18 Hz and this frequency is used for all noise data reported in the manuscript. Since the spectra are 1/*f*, the choice of octave frequency is arbitrary. Choosing a low frequency is advantageous in that it ensures the MR noise is large in comparison to the other (non-magnetic) noise sources.

Figure 4 plots the TMR and MR noise as a function of applied field. It is convenient to define a MR 1/*f* noise parameter as $\alpha_{mag} \equiv \Omega f S_V^{mag}/V^2$, where Ω is the volume of the

corresponding magnetic layer.[23] Using the FD theorem,[23] the magnetic noise can be related to the magnitude of the resistance susceptibility, $|\chi_R| = dR/dH$, namely,

$$\alpha_{mag} = \frac{\Omega f S_V^{mag}}{V^2} \approx \varepsilon(H) \frac{k_B T}{\pi \mu_0 M_s} \frac{\Delta R}{R} \left(\frac{1}{R} \frac{dR}{dH} \right), \quad (1)$$

where ΔR is the resistance change between the AP and the P state, $\mu_0 M_s$ is the saturation magnetization of the FM layer, $\varepsilon(H) \approx \chi_R'' / \chi_R'$ is the phase lag associated with magnetic losses, and the other terms have their usual meaning. The saturation magnetization is taken to be 1.6 T for $Co_{40}Fe_{40}B_{20}$ and 1.76 T for $Co_{90}Fe_{10}$. We define the magnetoresistance-sensitivity product as $\text{MSP} \equiv (\Delta R / R^2)(dR/dH)$. Equation (1) shows that the MR 1/*f* noise is proportional to the product of the MSP and the phase lag which in turns depends on materials properties.

Equation (1) assumes that only one magnetic layer is fluctuating, the other being effectively pinned. Previous work[17,20-24] has shown that this is often the case in regions of the TMR curve where either the free or the reference layer is undergoing magnetic reversal. At intermediate fields, corresponding to the AP state on the TMR plot, it is more likely that both layers fluctuate simultaneously, which results in more MR noise than is predicted by Eq. (1). The field range over which this excess MR noise is observed can be seen in Fig. 4 as the region between the two noise peaks due to the reversals the free and reference layers where α_{mag} is field independent. Other reports have noticed this feature for MgO-based MTJs.[27,28] Excess magnetic noise in the AP state was also found by Hardner *et al*.[29] in Co/Cu bilayers. They attributed the breakdown of this single-layer model to defects in the AP ordering. Here, we are concerned primarily with the reference layer and we assume that the magnetization in the free layer is pinned. In our analysis of the reference layer's noise, we exclude data over that portion of the AP state where both layers may be fluctuating and leading to excess MR noise. The range of

fields corresponding to the AP state varies among devices. In Fig. 4(a), the noise and resistance of S1 after 20 s of annealing at 380 °C are relatively field-independent from −4 to −16 mT. Figure 4(b) shows two distinct noise peaks with a small field-independent region in between the two from −10 to −20 mT for S5. Equation (1) can only be applied to regions in the AP state over which the TMR plot exhibits some field dependence.

In general, the magnetic field dependence of α_{mag} exhibits two peaks. Such peaks are evident in Fig. 5(a) which shows noise data for S1 after 2600 s of annealing at 380 °C. The narrower noise peak near zero field corresponds to the reversal of the free layer as indicated by the fast switching from low to high resistance in the TMR curve in Fig. 5(c). The rounded peak centered at $H = H_{\Lambda}$ represents the reference layer. The leftmost vertical dashed line denotes, H_{ref}, the external field at which the MSP due to the reference layer is a maximum. For all devices measured, the magnitude of H_{Λ} was a few milliteslas smaller than H_{ref}. All data in Fig. 3 was taken at H_{ref} in order to characterize the behavior of the MR $1/f$ noise at maximum sensitivity. The spectra shown in Fig. 3 are for MTJs having different strengths of exchange bias coupling (see Table II). It is evident that a $1/f$ spectrum is a general characteristic; that is, the spectral slope is not dependent on the strength of the exchange bias. Since the reference layer is exchange-biased and the free layer is not, the magnetic field dependence of the MSP for those two layers display different profiles as can be seen in Fig. 5(b). For the reference layer, MSP(H) exhibits a broad, asymmetric peak which has a maximum value less than that of the sharply peaked free layer. Similar field dependences have been reported in the resistance susceptibility.[23]

Figure 6 plots the field profiles of both α_{mag} and MSP for S1 with the same number of decades. A linear correlation between these two quantities is clearly evident over some range of

fields. In Fig. 6(a), MSP and α_{mag} track one another in the field ranges of −16 to −25 mT and −40 to −70 mT. Figure 5(c) shows that −16 to −25 mT corresponds to the AP state and −40 to −70 mT to the P state.

The data in Fig. 6(a) is for S1 after it was thermally annealed at 380 °C for 2600 s. Figure 6(b) shows similar data for the same device after it has been subjected to a thermal treatment at 380 °C for 173000 s. A comparison of the field profiles of the MSP reveals that the effect of prolonged thermal annealing is to shift the reference layer's peak towards zero field and to sharpen it. The result is that the shape of the reference layer's MSP peak closely resembles that of the free layer's and the entire MSP(H) curve takes on the shape of the letter 'M'. The shift toward zero field also indicates that annealing reduces the strength of the exchange bias coupling.

Having determined $\alpha_{mag}(H)$ and MSP(H), Eq. (1) can be used to calculate the phase lag $\varepsilon(H)$. ε is materials-dependent and it reflects the magnetic losses. Through its field dependence we can investigate the properties of the free and reference layers. $\varepsilon(H)$ will be independent of field if $\alpha_{mag}(H)$ and MSP(H) are linearly correlated. Figure 6 shows that this is mostly the case over the range of fields extending from +40 mT to small negative fields, which includes the reversal of the free layer. When the correlation is not linear, $\varepsilon(H)$ becomes field-dependent. From −20 to −71 mT in Fig. 6(b), α_{mag} has a steeper slope than the MSP during the magnetic reversal of the reference layer, indicating that a linear correlation between them is no longer present.

To gain better insight into the field dependence of ε, Fig. 7 plots α_{mag} as a function of MSP over a range of fields corresponding to the magnetic reversal of the reference layer. Data is shown for S1 after 2600 s and excludes fields ranging from 0 to −16 mT where there is excess

MR noise. The solid diagonal lines in Fig. 7 depict values of constant ε (in degrees). In the P and AP states, α_{mag} exhibits a linear dependence on MSP indicating that ε is constant. During the magnetic reversal, ε is field-dependent. The locations of the characteristic fields corresponding to the maximum amplitude of α_{mag} and MSP are indicated by H_Λ and the intersection of the dashed line with the symbols (H_{ref}), respectively. α_{mag} is a multi-valued function of MSP. ε is more than a factor of 10 larger before the reversal than it is after the reversal. During the magnetic reversal of the reference layer, ε is field-dependent with its highest value of 1.5 ° corresponding to the AP state (−16 to −25 mT) and its lowest value of 0.1 ° in the P state (−40 to −70 mT).

To study the magnetic losses of the reference layer, we select the field at which MSP(H) exhibits a maximum value, that is, at H_{ref}. The magnetic losses at $H_{ref} \approx -30$ mT are then parameterized by the quantity $\varepsilon_{ref} = \varepsilon(H=H_{ref})$ which equals 0.51°. There are other characteristic fields at which one can study the reference layer including: the MR noise peak at H_Λ and the exchange anisotropy field at H_{ex}. However, we found that the corresponding phase lags at these fields do not show systematic trends, for instance, with increased annealing time. Annealing changes the shapes of the TMR and MSP(H) curves and the values of H_{ref}, H_Λ, and H_{ex}. Hence, the relative positions along the TMR and MSP(H) curves corresponding to these fields will also change. Since the phase lag is field-dependent, particularly in the magnetic reversal region, its value measured at H_Λ and H_{ex} tends to show complex behavior as the corresponding positions shift along the TMR and MSP(H) curves. On the other hand, H_{ref} always corresponds to the maximum of the MSP(H) curve even when the profile of that curve changes with increased annealing time. Parameterizing the magnetic losses at H_{ref} is also a logical choice from the perspective of applications since that is the likely operating point of a magnetic field sensor.

Figure 8 plots $\varepsilon(H)$ for S1 after three different annealing times. Although the field dependence is non-trivial, a general trend found at all annealing times and amongst all devices is that ε has a larger value in the AP state. Inspection of Fig. 8 also reveals a large reduction in ε at higher annealing times. After 20 and 2600 s of annealing, we find that TMR has been increased by a factor of 5 (from 40.3 % at 20 s to 203 % at 2600 s) but ε_{ref} and H_{ref} maintain their values around 0.5 ° and –30 mT, respectively. After 173000 s, the TMR has increased further to 285 %, but now a significant decrease in H_{ref} is evident and a factor of 5 reduction in ε_{ref}. The rise in ε at large negative fields for 20 s is attributed to a poor magnetic microstructure at such a low annealing time. For this reason 2600 s may be considered as the optimal annealing time. Around this time, the device displays the largest TMR without losing exchange bias coupling. The data for the three annealing times suggest that a relation exists between ε_{ref} and H_{ref} (the strength of the exchange bias coupling).

Thermal annealing also has pronounced effects on the shape of that portion of the TMR curve associated with the magnetic reversal of the reference layer, as evidenced in Fig. 8. The dashed lines in Fig. 8 denote H_{ref}, the magnetic field at which MSP exhibits a maximum. This field is approximately the field at which the slope of the TMR curve is largest. For 20 and 2600 s the position of H_{ref} along the TMR curve is nearly the same and located close to or above the midpoint. The largest time of 173000 s shows the location is much farther down on the TMR curve. To parameterize this dependence we define an exchange factor, $E \equiv \mathrm{TMR}(H_{ref})/\mathrm{TMR}_{max}$. E can be considered as a measure of the quality of the exchange bias between the AF layer and the reference layer. For comparison, the exchange anisotropy field, H_{ex}, is defined as the external field at which TMR becomes half of its maximum value.[12] For instance, if $H_{ref} = H_{ex}$, then $E = 0.5$. We find that devices with the strongest exchange bias coupling tend to have values

of E around 0.5. For example, Fig. 9 shows that E remains above 0.5 for S1 at short annealing times and drops monotonically with increased annealing time. Similar behavior is observed for devices S2, S3, and S4. In earlier work, we showed that MSP increases with annealing time.[24] The inset of Fig. 9 plots E versus MSP for the reference layers of devices S1 through S4. It can be seen that E is a decreasing function of MSP. After 10^4 s of annealing at 380 °C, S1 and S4 show the smallest values of E with 0.217 and 0.189 but the largest MSP values with 0.609 and 0.384 mT^{-1}.

Thermal annealing also alters the magnetic field dependence of MSP for the reference layer, making it sharper and more symmetric about H_{ref} with increased annealing time. The evolution of the MSP's field profile is shown in Fig. 10 which plots MSP, normalized by its maximum value, as a function of $H–H_{ref}$. Positive (negative) fields correspond to before (after) the reversal of the reference layer. At short annealing time (< 2600 s), MSP is asymmetric with a pronounced flat region about the maximum. However, at longer times (> 19000 s) it becomes sharper and more symmetric, approaching a triangular shape. These triangular profiles resemble those of the free layer; see, for example, Fig. 6. Summarizing, we observe that as the strength of the exchange bias coupling decreases, the shape of the magnetic profile of the reference layer approaches that of the free layer. This is perhaps expected since in the limit of no exchange bias, the reference layer should behave like the magnetically soft free layer.

DMTJ devices are useful for comparing top and bottom pinning configurations under identical annealing conditions. In DMTJs, α_{mag} and MSP exhibit three peaks which are associated with reversals of the free layer and the two reference layers. These peaks can be seen in Fig. 11(a) and (b). The two vertical dashed lines again represent H_{ref} for the two pinning configurations. In Fig. 11(b), the sharp peak at zero field signifies the free layer reversal, the one

at −28 mT is the top-pinned reference layer, and the other at −80 mT is the bottom-pinned reference layer. Since the bottom-pinned reference layer switches at more negative fields, its exchange bias coupling is stronger than the top pinning configuration. The phase lag, $\varepsilon(H)$, is plotted in Fig. 11(c). The bottom-pinned reference layer has a larger value of $\varepsilon_{ref} = 1.4$ ° than the top-pinned layer which has $\varepsilon_{ref} = 0.68$ °.

The TMR curve of DMTJs shows a two-step decline from the AP to P state at negative fields due to the reversal of both reference layers. For DMTJs, the contributions of the two reference layers to the TMR must be separated in order to calculate their respective values of E. This involves finding the region of the TMR curve in Fig. 11(c) in which both the free and top-pinned reference layer have undergone a reversal but where the bottom one has not. This region is used to assign the maximum TMR for the bottom-pinned reference layer and minimum TMR for the top (163 % at −40 mT). We find that the value of E for bottom and top pinning configurations are 0.50 and 0.56, respectively.

In Table II we list a number of relevant quantities for each of the devices. Examination of Table II reveals a correlation between ε_{ref} and H_{ref}. For devices having a TMR value greater than 150 %, we find that ε_{ref} decreases systematically as the magnitude of H_{ref} decreases. For instance, for S1 after 173000 s of annealing, we find $\varepsilon_{ref} = 0.10$ ° at $H_{ref} = -19.3$ mT whereas for S6 $\varepsilon_{ref} = 1.44$ ° at $H_{ref} = -69.8$ mT. Figure 12 is a compilation plot of MSP and ε_{ref} as a function of H_{ref} for a number of devices. The general trend that emerges is one where MSP increases as H_{ref} approaches zero field. Since the magnetic losses are calculated from Eq. (1), most of the dependence of ε_{ref} on H_{ref} comes from dependence of MSP on H_{ref}, rather than from α_{mag}. Finally, we note the dashed line in Fig. 12 which is used to delineate MTJs with a seed layer thickness above and below 3 nm. The scatter on the right side of the dashed line in Fig. 12

represents device-to-device variation of three MTJs at multiple annealing times, all having a seed layer thickness of 2 nm. Measurement reproducibility, on the other hand, corresponds to the vertical size of the data symbols.

The results reported for ε_{ref} and H_{ref} depended very weakly on bias conditions. In Fig. 13, we plot the field dependence of ε and TMR at different current biases of S1 after 85000 s of annealing. Clearly, the TMR decreases at higher biases from 280 % at 357 μA to 178.2 % at 3.57 mA. However, the field profile of ε throughout the reversal of the reference layer remains the same along with the magnitude of H_{ref}. Values for ε_{ref} are 0.11 ° at 357 μA and 0.135 ° at 3.57 mA.

IV. DISCUSSION

Exchange bias is important for engineering desirable magnetic properties into spin-electronic devices. These properties include distinct switching fields for the magnetically soft and hard layers of a device. Dieny *et al*.[8] noted that the use of exchange bias in sandwiches consisting of two uncoupled FM layers separated by a NM metal expanded the study of MR effects to new and wide-ranging class of materials. Exchange biasing does, however, add complexity to the materials stack, typically requiring additional layers. Our data indicate that the MR noise associated with the reference layer is related to and affected by the exchange bias. Specifically, the parameter used to quantify the magnetic losses in the reference layer (i.e., ε_{ref}) decreases as the exchange bias field is reduced, either through degradation from thermal treatments or by varying the thickness of the underlying seed layer on which the AF is grown.

In the limit of no exchange bias, the reference layer should behave like the free layer. The free layer and reference layer with the weakest exchange bias coupling have similarities not

only in the value of the phase lag but also in their magnetic field dependence of MSP. For example, Fig. 8 shows that the phase lag of S1's free layer is about 0.05 ° which is only a factor of 2 smaller than ε_{ref} after 173000 s of annealing. When the exchange bias is severely reduced through prolonged annealing, there is a reduction in H_{ref}, H_{ex}, and H_{Λ}.[24] As a result, the MSP(H) curve for the reference layer resembles the free layer as shown in Fig. 10. This sharp peak in MSP suggests a trend towards a more magnetically soft layer. In contrast, prolonged annealing has little effect on the losses in the free layer. For example, the phase lag for the S1's free layer is independent of annealing time from 2600 s to 173000 s while ε_{ref} decreases by a factor of 5 in that same period. This suggests that the factor of 5 decrease in ε_{ref} is correlated to the reduction in exchange bias.

Using Lorentz microscopy, Shaw *et al.*[15] found that isolated magnetic layers had far less magnetic disorder and magnetization ripple than a free layer in a multilayer MTJ structure. Their results suggest that disorder originates in the exchange bias layer and gets imprinted on the free magnetic layer by local magnetostatic coupling. Moreover, dynamic Lorentz imaging revealed Barkhausen jumps in the magnetic microstructure on the scale of the average ripple wavelength. These discrete jumps could be a source of low-frequency MR noise. It is plausible that disorder and ripple contribute to the MR noise we observe from the reference layer. This disorder may get transferred from the AF layer to the reference layer by exchange coupling. The disorder in the AF layer may in turn be due to the type and thickness of the underlying seed layer.

It is well known that the seed layer is very influential in determining the texture in the AF layer. van Driel *et al.*[13] observed that the removal of the Ta seed layer prompted a strong decrease of the (111) texture in IrMn and loss of exchange bias coupling. Also, Wiśniowski *et al.*[14] studied how the seed layer impacted the texture, roughness, exchange bias coupling, and

magnetic domain structure of MTJs. X-ray diffraction and atomic force microscopy measurements were used to determine the degree of texture and roughness of IrMn(111) between two types of seed layers. They found that high texture and increased interfacial roughness were associated with larger grains that grew in the form of columns oriented perpendicular to the substrate. Highly textured buffer layers resulted in larger exchange bias coupling along with pronounced magnetic ripple patterns. Based on these works and our results shown in Fig. 12, we conclude that devices with larger exchange bias coupling have greater magnetic disorder and higher losses.

Relatedly, the thickness of the seed layer also plays a role in determining magnetic losses; we find that H_{ref} and ε_{ref} decrease with decreasing thickness of the seed layer. DMTJs best illustrate this point since two types of pinning configurations are employed using different seed layer thicknesses while the entire materials stack is subject to the same annealing conditions. A 5 nm thick NiFe seed layer is used for bottom-pinning and a 2.5 nm thick CoFe seed layer is used for top-pinning. This difference results in different exchange bias fields for the two reference layers. Previously, it was shown that bottom-pinned reference layers in MTJs having single and double barriers with the same exchange bias layers exhibit the same values for H_{ex} whereas top-pinned reference layers have smaller values of H_{ex}.[30,31] A plausible explanation is that a thicker seed layer (above ~ 3 nm) induces greater (111) texture in the AF layer which results in higher H_{ex}.

To illustrate this point further, Table II lists several devices, with different stack structures but similar seed layer thicknesses, having comparable values for ε_{ref} and H_{ref}. For example, the top-pinned reference layer of S9 with a 2.5 nm thick seed layer of CoFe has values for ε_{ref} and H_{ref} that are roughly the same as bottom-pinned reference layers of S1 through S4

where the seed layers are 2 nm thick. Also, the bottom-pinned reference layers of S7 through S9 with a 5 nm thick NiFe seed layer are similar to S6 which has a 4 nm thick CoFe seed layer. Finally, the top-pinned S10 with a 3.5 nm seed layer of CoFe has characteristics similar to the bottom-pinned S5 with a 4 nm seed layer of CoFe.

In this work we have shown that the incorporation of exchange bias layers leads to increased low-frequency MR noise at fields corresponding to the reversal of the reference layer. Studies by You *et al*.[32] indicate that exchange bias layers can also lead to increased thermal magnetic noise at much higher frequencies. Their work revealed extra resonance peaks in the magnetic noise spectra in the GHz range, which represent the thermal motion of the reference layer spins. Evidently, the use of exchange bias can lead to increased magnetic noise at both very low and very high frequencies.

Exchange bias layers, together with shape anisotropy[33] or the application of a hard-axis bias field,[34] are often used in magnetic sensors to provide a linear sensing region. One alternative is to magnetically pin both the top and bottom electrodes in orthogonal directions by using AF layers.[35,36] Recently, Chen *et al*.,[36] fabricated such a device using MTJs with a MgO tunnel barrier. Their devices exhibited TMR values above 200 % along with a linear sensing region and high sensitivity. However, a drawback of having two exchange-biased layers is enhanced noise from the sensing layer, which can be seen in Fig. 3(a) in Ref. 36 to extend far into the P state.

In addition to influencing the MR noise, the incorporation of exchange bias into a materials stack also affects the signal, i.e., the TMR. Examination of our data and data in the literature[24,30,37,38] reveals a correlation between TMR and the magnitude of the exchange bias field, namely, higher TMR is found in devices having lower H_{ex}. In exchange-biased MTJs,[12,39]

for example, when the TMR was above 350 % the magnitude of H_{ex} was below 15 mT. In other devices having H_{ex} > 50 mT, smaller TMR values, below 225 %, were observed.[40] Devices having among the highest reported TMR values (> 600 %) are pseudo-SV MTJs, which do not use exchange bias layers.[10]

Caution is required, however, when drawing conclusions from comparisons of devices made by different research groups because the TMR is affected by a number of factors which can vary between groups, such as: differences in materials stacks, and thin film deposition conditions and annealing treatments. To mitigate some of these differences, we examine devices with the same materials stack structure and annealing treatment. Figure 14 depicts the relationship between the TMR and H_{ex} for devices S1, S3, and S4 measured at successively longer annealing times. In these devices, the strength of the exchange bias weakens as the cumulative annealing time increases. Concomitant with the decrease in exchange bias is an increase in TMR. Figure 14 also includes similar data extracted from Fig. 1(a) in Ref. 41. We have plotted their data at 90 and 315 s for an annealing temperature of 500 °C. The data shows the TMR increasing from 285 % after 90 s to 310 % after 315 s, and that the exchange bias has dropped down to 9 mT after 315 s. It appears that high annealing temperatures of 500 °C or greater[10] are necessary to achieve a TMR value larger than 300 % but at the cost of severely weakening the exchange bias.

Additional evidence in support of the inverse correlation between TMR and H_{ex} comes from the work of Kurt *et al*.[37] in which TMR curves are reported at different annealing temperatures. Their data shows that the TMR increases from 212 % to 240 % and that H_{ex} decreases from 45 mT to 35 mT when the annealing temperature is increased from 375 to 425 °C. Their MTJs had the same materials stack structure as S7 and S8 with 5 nm-thick seed layers of NiFe. The important aspect of this work is that the authors found the same behavior for two

types of nominally identical MTJs structures, differing only in whether the MgO tunnel barrier was grown by rf sputtering or by electron-beam evaporation. The latter growth technique was shown to produce MgO barriers having a smaller density of oxygen vacancies. Hence, one may infer that the magnetics (i.e., H_{ex}) are as important as barrier quality in determining the value of TMR; at least for MgO-based MTJs that exhibit high TMR (> 200 %).

The origin of the correlation between TMR and H_{ex} in MgO-based MTJs may be due to a competition between different microstructures among the various layers in the materials stack: one that promotes strong exchange bias coupling and another that leads to coherent tunneling and large TMR. The microstructure of the various layers in a materials stack depends in turn on the choice and thickness of the underlying seed layer. For instance, Cao *et al*.[42] found that the texture of the seed layer impacts the crystallization of the bottom electrode in MgO-based MTJs. A 20 nm thick Ta seed layer with (200) texture induced the growth of (001) oriented grains in the PtMn AF layer. These grains led to the crystallization of the bottom CoFeB electrode having a (200) orientation and resulted in a TMR of 290 %. On the other hand, a 3 nm thick Ta seed layer with (110) texture induced a (111)-oriented fcc texture into AF layer. This texture served as a template upon which the bottom electrode is grown and resulted in a lower TMR value of 200 %. From the curvature of the TMR(H) curve near the AP state we infer that MTJs with the thicker Ta seed layer and larger TMR have a lower value for H_{ex} than devices having strong (111) texture in the PtMn layer. Devices with strong (111) texture have TMR curves that exhibit negligible field dependence near the AP state.

In multilayer structures such as MTJs, magnetic disorder in the underlying AF layer can propagate upwards to the free layer[15] and have a deleterious impact on the TMR value. Intermediate layers, such the NM metal spacer layer found in SAFs can also affect the transport

properties, particularly in MgO-based MTJs. For comparison, the texture of the seed layer was shown to increase the TMR from 200 to 290 % by promoting a (200) orientation in the reference layer[42] while the presence of the spacer layer was found to increase the TMR from 181 to 361 % for the same reason.[12]

Equation 1 indicates that the MR noise is proportional to the product of the MSP and the magnetic losses. Hence, noise can be used to infer information related to the magnetization dynamics in the system. Our studies of low-frequency MR 1/*f* noise from the reference layer reveal that a decrease in the magnetic losses (noise) and an increase in the TMR (signal) are correlated to a reduction in the strength of the exchange bias. The strength of the exchange coupling is dependent on the texture of the seed layer and the annealing conditions. Put simply, a seed layer texture that gives rise to a stronger exchange bias coupling introduces a larger degree of magnetic disorder in the reference tunneling electrode which results in higher losses (noise) and decreased TMR (signal). Recognizing that exchange bias and magnetic disorder can adversely affect the signal-to-noise ratio is important in applications of exchange-biased MTJ devices

V. CONCLUSION

We have measured the influence of exchange bias on the low-frequency magnetic losses of the reference layer in sputtered-deposited and electron-beam evaporated CoFeB/MgO/CoFeB tunnel junctions near maximum resistance susceptibility and how the losses depend upon the thickness of the underlying seed layer and the thermal annealing treatment. Higher magnetic losses and greater exchange bias fields were found in devices having thicker seed layers. Results in DMTJs, which have different top and bottom pinning configurations, confirmed the relation

between the thickness of the seed layer and its magnetic losses. Increased annealing time reduced the exchange bias field which resulted in an increase in resistance susceptibility and a decrease in magnetic losses. With a weakened exchange bias, the field dependence of resistance susceptibility of the reference layer begins to resemble that of the free layer – characterized by a sharp, symmetric peak. Moreover, the phase lag of the reference layer (ε_{ref}) in devices with the weakest exchange bias becomes comparable to that of the free layer. Thermal annealing had little impact on the magnetic losses of the free layer. Other reports[14,15] have linked large exchange bias coupling created by a strong (111) texture in the AF layer to large amounts of magnetic disorder and ripple in the magnetic microstructure. We attribute the observed correlation between the value of ε_{ref} and strength of exchange bias to the underlying magnetic disorder in the FM layers of the device. In contrast, increased disorder leads to an inverse correlation between the TMR and the strength of the exchange bias.

For applications, such as magnetic field sensors, we anticipate that compromises will arise between the desire for large and robust exchange bias and the need to maintain high TMR (signal) and low losses (noise). Finally, this work demonstrates that magnetic losses determined from measurements of MR 1/*f* noise can be used to probe magnetic disorder in magnetic layers that are buried within a multilayer structure and otherwise not easily imaged directly using Kerr[14] or Lorentz microscopy.[15]

ACKNOWLEDGEMENTS

At CRANN and School of Physics at Trinity College in Dublin, Ireland we thank H. Kurt for fabrication of S7 and S8 and G. Q. Yu and Z. Diao for providing data for S9. At the University of Delaware, we are grateful to K. M. Haughey and A. Ozbay for providing data for S10 and S11 and L. R. Shah for annealing treatment of S1 through S4. This work was supported by the DOE under Award No. DE-FG02-07ER46374. The work of R. S. was supported in part by NASA's Delaware Space Grant program.

REFERENCES

1. W. H. Meiklejohn and C. P. Bean, Physical Review **105**, 904 (1957).
2. M. N. Baibich, J. M. Broto, A. Fert, F. Nguyen Van Dau, and F. Petroff, Physical Review Letters **61**, 2472 (1988).
3. G. Binasch, P. Grünberg, F. Saurenbach, and W. Zinn, Physical Review B **39**, 4828 (1989).
4. A. Chaiken, G. A. Prinz, and J. J. Krebs, Journal of Applied Physics **67**, 4892 (1990).
5. P. Grünberg, R. Schreiber, Y. Pang, M. B. Brodsky and H. Sowers, Physical Review Letters **57**, 2442 (1986).
6. S. S. P. Parkin, N. More, and K. P. Roche, Physical Review Letters **64**, 2304 (1990).
7. C. Dupas, P. Beauvillain, C. Chappert, J. P. Renard, F. Trigui, P. Veillet, E. Vélu, and D. Renard, Journal of Applied Physics **67**, 5680 (1990).
8. B. Dieny, V. S. Speriosu, S. S. P. Parkin, B. A. Gurney, D. R. Wilhoit, and D. Mauri, Physical Review B **43**, 1297 (1991).
9. David D. Djayaprawira, Koji Tsunekawa, Motonobu Nagai, Hiroki Maehara, Shinji Yamagata, Naoki Watanabe, Shinji Yuasa, Yoshishige Suzuki, and Koji Ando, Applied Physics Letters **86**, 092502 (2005).
10. S. Ikeda, J. Hayakawa, Y. Ashizawa, Y. M. Lee, K. Miura, H. Hasegawa, M. Tsunoda, F. Matsukura, and H. Ohno, Applied Physics Letters **93**, 082508 (2008).
11. X.-G. Zhang and W. H. Butler, Physical Review B **70**, 172407 (2004).
12. Y. M. Lee, J. Hayakawa, S. Ikeda, F. Matsukura, and H. Ohno, Applied Physics Letters **89**, 042506 (2006).

13. J. van Driel, F. R. de Boer, K.-M. H. Lenssen, and R. Coehoorn, Journal of Applied Physics **88**, 975 (2000).

14. P. Wiśniowski, T. Stobiecki, J. Kanak, G. Reiss, H. Brückl, Journal of Applied Physics **100**, 013906 (2006).

15. Justin M. Shaw, Roy Geiss, and Stephen Russek, Applied Physics Letters **89**, 212503 (2006).

16. W. F. Egelhoff Jr, P. W. T. Pong, J. Unguris, R. D. McMichael, E. R. Nowak, A. S. Edelstein, J. E. Burnette, and G. A. Fischer, Sensors and Actuators A: Physical **155** (2), 217 (2009).

17. G. Q. Yu, Z. Diao, J. F. Feng, H. Kurt, X. F. Han, and J. M. D. Coey, Applied Physics Letters **98**, 112504 (2011).

18. Ryan Stearrett, W. G. Wang, L. R. Shah, Aisha Gokce, J. Q. Xiao, and E. R. Nowak, Journal of Applied Physics **107** (6), 064502 (2010).

19. J. M. Almeida, P. Wisniowski, and P. P. Freitas, IEEE. Trans. Magn. **44**, 2569 (2008).

20. L. Jiang, E. R. Nowak, P. E. Scott, J. Johnson, J. M. Slaughter, J. J. Sun, and R. W. Dave, Physical Review B **69** (5), 054407 (2004).

21. Cong Ren, Xiaoyong Liu, B. D. Schrag, and Gang Xiao, Physical Review B **69** (10), 104405 (2004).

22. Xiaoyong Liu, Cong Ren, and Gang Xiao, Journal of Applied Physics **92**, 4722 (2002).

23. A. Ozbay, A. Gokce, T. Flanagan, R. A. Stearrett, E. R. Nowak, and C. Nordman, Applied Physics Letters **94** (20), 202506 (2009).

24. Ryan Stearrett, W. G. Wang, L. R. Shah, J. Q. Xiao, and E. R. Nowak, Applied Physics Letters **97**, 243502 (2010).

25. Zhu Diao, E. R. Nowak, K. M. Haughey, and J. M. D. Coey, Physical Review B **84**, 094412 (2011).

26. Arif Ozbay, E. R. Nowak, A. S. Edelstein, G. A. Fischer, C. A. Nordman, and Shu Fan Cheng, IEEE Transactions on Magnetics **42**, 3306 (2006).

27. H. Duan, H. W. Tseng, Y. Li, and R. B. van Dover, Journal of Applied Physics **109**, 113917 (2011).

28. R. Guerrero, F. G. Aliev, R. Villar, J. Hauch, M. Fraune, G. Güntherodt, K. Rott, H. Brückl, and G. Reiss, Applied Physics Letters 87, 042501 (2005).

29. H. T. Hardner, M. B. Weissman, M . B. Salamon, and S. S. P. Parkin, Physical Review B **48**, 16156 (1993).

30. G. Feng, Sebastiaan van Dijken, J. F. Feng, J. M. D. Coey, T. Leo, and David J. Smith, Journal of Applied Physics **105**, 033916 (2009).

31. H. D. Gan, S. Ikeda, W. Shiga, J. Hayakawa, K. Miura, H. Yamamoto, H. Hasegawa, F. Matsukura, T. Ohkubo, K. Hono, and H. Ohno, Applied Physics Letters **96**, 192507 (2010).

32. Chun-Yeol You, Jungbum Yoon, Seung-Young Park, Shinji Yuasa, Myung-Hwa Jung, Current Applied Physics **11**, e92 (2011).

33. Y. Lu, R. A. Altman, S. A. Rishton, P. L. Trouillound, G. Xiao, W. J. Gallagher, and S. S. P. Parkin, Applied Physics Letters **70**, 2610 (1997).

34. Mark Tondra, James M. Daughton, Dexin Wang, Russell S. Beech, Anita Fink, and John A. Taylor, Journal of Applied Physics **83**, 6688 (1998).

35. B. Negulescu, D. Lacour, F. Montaigne, A. Gerken, J. Paul, V. Spetter, J. Marien, C. Duret, and M. Hehn, Applied Physics Letters **95**, 112502 (2009).

36. J. Y. Chen, J. F. Feng, and J. M. D. Coey, Applied Physics Letters **100**, 142407 (2012).

37. H. Kurt, K. Oguz, T. Niizeki, and J. M. D. Coey, Journal of Applied Physics **107**, 083920 (2010).

38. J. Hayakawa, S. Ikeda, Y. M. Lee, F. Matsukura, and H. Ohno, Applied Physics Letters **89** (23), 232510 (2006).

39. Shinji Yuasa, Akio Fukushima, Hitoshi Kubota, Yoshishige Suzuki, and Koji Ando, Applied Physics Letters **89**, 042505 (2006).

40. Z. Diao, J. F. Feng, H. Kurt, G. Feng, and J. M. D. Coey, Applied Physics Letters **96**, 202506 (2010).

41. W. G. Wang, C. Ni, G. X. Miao, C. Weiland, L. R. Shah, X. Fan, P. Parson, J. Jordan-sweet, X. M. Kou, Y. P. Zhang, R. Stearrett, E. R. Nowak, R. Opila, J. S. Moodera, and J. Q. Xiao, Physical Review B **81**, 144406 (2010).

42. J. Cao, J. Kanak, T. Stobiecki, P. Wisniowski, and P. P. Freitas, IEEE Transactions on Magnetics **45**, 3464 (2009).

FIGURE CAPTIONS

FIG. 1. Room temperature magnetization (a) and TMR (b) for an exchange-biased MTJ as a function of the applied field swept from 250 to −250 mT. The relative orientations of these two layers are designated by the pairs of arrows in each region of the *M-H* curve.

FIG. 2. (Color online) Illustration of stack structures for GMR SV, MTJ, and DMTJ. The reference layer in GMR SVs is the pinned layer due to the lack of a SAF structure. In addition, the seed layer for the top pinning configuration of GMR SV and DMTJ is the pinned layer since the AF layer is grown on top of the pinned layer.

FIG. 3. (Color online) Normalized MR 1/*f* noise taken at maximum sensitivity of the reference layer as a function of frequency for four different MTJs with variation in its strength of exchange bias. The annealing time of 85000 s of S1 corresponds to the 357 μA bias data in Table II. S6 does not have data for frequencies of 144 and 288 Hz because the thermal noise of the MTJ dominates due to its high resistance (70 kΩ in the P state).

FIG. 4. (Color Online) α_{mag} (symbols) and TMR (solid lines) are plotted as a function of the applied field for S1 at 20 s in (a) and for S5 in (b). Both S1 and S5 have been annealed at 380 °C. The elevated noise in the AP state is shown for both panels. We note that the noise at positive fields in panel (a) is electronic in nature and is not shown.

FIG. 5. (Color online) The magnetic field dependence of α_{mag}, MSP, ε, and TMR of S1 after 2600 s of annealing at 380 °C. The field sweep from 40 to −70 mT has the reference

layer undergo a transition from the AP to P state. In panel (c), the symbols (solid lines) represent ε (TMR) while the dashed lines represent the MR noise peak at H_Λ and the MSP peak at H_{ref} of the reference layer. The magnetic losses associated with the reference layer are largest for the AP state.

FIG. 6. (Color online) Annealing time dependence of α_{mag} (symbols) and MSP (solid lines) of S1 as a function of the applied field for 2600 s (a) and 173000s (b). The reference layer has an 'M'-shaped MSP curve after 173000 s of annealing, which demonstrates the weakened exchange bias. Both annealing times have a constant current bias of 357 μA.

FIG. 7. (Color online) The dependence of the MR noise on MSP for a field range of −15.5 to −70 mT from Fig. 5. The dashed line represents H_{ref} and solid lines represent constant magnetic losses at 300 K.

FIG. 8. (Color online) Annealing time dependence of ε (symbols) and TMR (solid lines) of S1 as a function of the applied field. The dashed line in each panel represents H_{ref} at that annealing time.

FIG. 9. (Color online) The main panel illustrates the annealing time dependence of E for devices S1 through S4. The inset displays E as a function of MSP.

FIG. 10. (Color online) The annealing time dependence of the field profile for normalized MSP of S1. Higher annealing times show a magnetically soft behavior of the MSP peak for the reference layer.

FIG. 11 (Color online) The magnetic field dependence of α_{mag}, MSP, ε, and TMR of DMTJs. In panel (c), the symbols (solid lines) represent ε (TMR) while the dashed line

represents H_{ref} for both top and bottom pinning configurations. Data from Fig. 1 of Ref. 17.

FIG. 12. (Color online) MSP and ε_{ref} as a function of H_{ref} are shown for MTJs with a TMR value of 150 % or larger. The dashed line at −40 mT separates the MTJs with thin seed layers (< 3 nm) to the right of the line from ones with thick layers (> 3 nm) to the left.

FIG. 13. (Color online) The bias dependence of ε (symbols) and TMR (solid lines) as a function of the applied field of S1 after 85000 s of annealing at 380 °C. The dashed line represents H_{ref}.

FIG. 14. (Color online) TMR as a function of H_{ex} for S1, S3, S4, and MTJs from Ref. 41. All data is for annealing times in which the TMR is greater than 200 %.

TABLE CAPTIONS

Table I. Materials stack composition with thicknesses in nanometers.

Table II. Summary of details regarding the device structure and annealing conditions as well as the transport properties and exchange bias values used in order to characterize the magnetic losses responsible for the MR noise of the reference layer. T_a is the annealing temperature and t_a is the annealing time. Annealing time dependence is shown for devices S1 through S4. S1 and S7 have two datasets corresponding to different current biases for same annealing time and can be identified by their superscripts A through D in the annealing time column (A = 357 μA, B = 3.57 mA, C = 1.2 μA, D = 24 μA). The difference in current bias is a factor of 10 for S1 and a factor of 20 for S7. Data is shown for both top and bottom pinning configurations of S9.

Table I

Layer	S1 through S4	S5 and S6	S7 through S9
Capping	Ta 8/Ru 10	Ta 8/Ru 26	$Ni_{81}Fe_{19}$ 5/Ta 5/Ru 10 (S9) Ta 5/Ru 10 (S7 and S8)
Free	$Co_{40}Fe_{40}B_{20}$ 3	$Co_{40}Fe_{40}B_{20}$ 2	$Co_{40}Fe_{40}B_{20}$ 3
Barrier	MgO 1-1.5	MgO 2	MgO 2-2.5
Reference	$Co_{40}Fe_{40}B_{20}$ 3	$Co_{40}Fe_{40}B_{20}$ 4	$Co_{40}Fe_{40}B_{20}$ 3
Spacer	Ru 1.7	Ru 1.7	Ru 0.9
Pinned	$Co_{70}Fe_{30}$ 2	$Co_{70}Fe_{30}$ 3	$Co_{90}Fe_{10}$ 2.5
AF	$Ir_{24}Mn_{76}$ 15	$Ir_{24}Mn_{76}$ 15	$Ir_{22}Mn_{78}$ 10
Seed	$Co_{70}Fe_{30}$ 2	$Co_{70}Fe_{30}$ 4	$Co_{90}Fe_{10}$ 2.5 (top) $Ni_{81}Fe_{19}$ 5 (bottom)
Buffer	Ta 7/Ru 20/Ta 7	Ta 7/Ru 20/Ta 7	Ta 5/Ru 30/Ta 5
Substrate	Si/SiO_2	Si/SiO_2	Si/SiO_2

Layer	S10	S11
Capping	Ta 5	metal
AF	$Ir_{22}Mn_{78}$ 10	CrPtMn 32.5
Pinned	$Co_{90}Fe_{10}$ 3.5	CoFe 4.35
Barrier	Cu 2.4	Cu 2.75
Free	$Ni_{81}Fe_{19}$ 3.5/$Co_{90}Fe_{10}$ 5	NiFeCo 4.25/CoFe 1.25
Buffer	Ta 5	Ta 4/NiFeCo 3.5/Ta 5
Substrate	Si/SiO_2	Si/Si_3N_4

Table II

#	Seed (nm)	Pinning Config.	t_a (s)	T_a (°C)	TMR (%)	E	H_{ref} (mT)	ε_{ref} (deg)	α_{mag} (μm^3)	MSP (mT^{-1})
1	CoFe 2	Bottom	20	380	40	0.677	-30.7	0.61	6.5×10^{-11}	0.006
1	CoFe 2	Bottom	2600	380	203	0.477	-30.0	0.51	5.9×10^{-10}	0.064
1	CoFe 2	Bottom	85000[A]	380	280	0.225	-20.8	0.14	1.1×10^{-9}	0.432
1	CoFe 2	Bottom	85000[B]	380	178	0.390	-20.8	0.11	4.3×10^{-10}	0.217
1	CoFe 2	Bottom	173000	380	285	0.217	-19.3	0.10	1.1×10^{-9}	0.609
2	CoFe 2	Bottom	30	430	114	0.622	-34.9	0.53	2.2×10^{-10}	0.023
3	CoFe 2	Bottom	240	430	216	0.405	-31.3	0.46	6.3×10^{-10}	0.076
3	CoFe 2	Bottom	2580	430	258	0.294	-26.0	0.25	8.4×10^{-10}	0.186
4	CoFe 2	Bottom	25980	430	272	0.189	-18.0	0.12	8.0×10^{-10}	0.384
5	CoFe 4	Bottom	167000	380	114	0.341	-41.7	0.56	5.7×10^{-10}	0.057
6	CoFe 4	Bottom	120	460	168	0.528	-69.8	1.44	5.2×10^{-10}	0.020
7	NiFe 5	Bottom	3600[C]	400	222	0.490	-59.4	1.34	4.3×10^{-10}	0.018
7	NiFe 5	Bottom	3600[D]	400	131	0.680	-59.5	1.28	2.3×10^{-10}	0.010
8	NiFe 5	Bottom	2280	380	190	0.487	-50.2	0.96	3.8×10^{-10}	0.022
9	NiFe 5	Bottom	3600	375	201	0.495	-80.0	1.40	4.8×10^{-10}	0.019
9	CoFe 2.5	Top	3600	375	201	0.555	-28.1	0.68	9.3×10^{-11}	7.6×10^{-3}
10	CoFe 3.5	Top	N/A	N/A	5.9	0.460	-45.3	0.64	1.7×10^{-12}	1.6×10^{-4}
11	CoFe 4.4	Top	N/A	N/A	3.0	0.586	-24.4	0.24	3.0×10^{-13}	7.7×10^{-5}

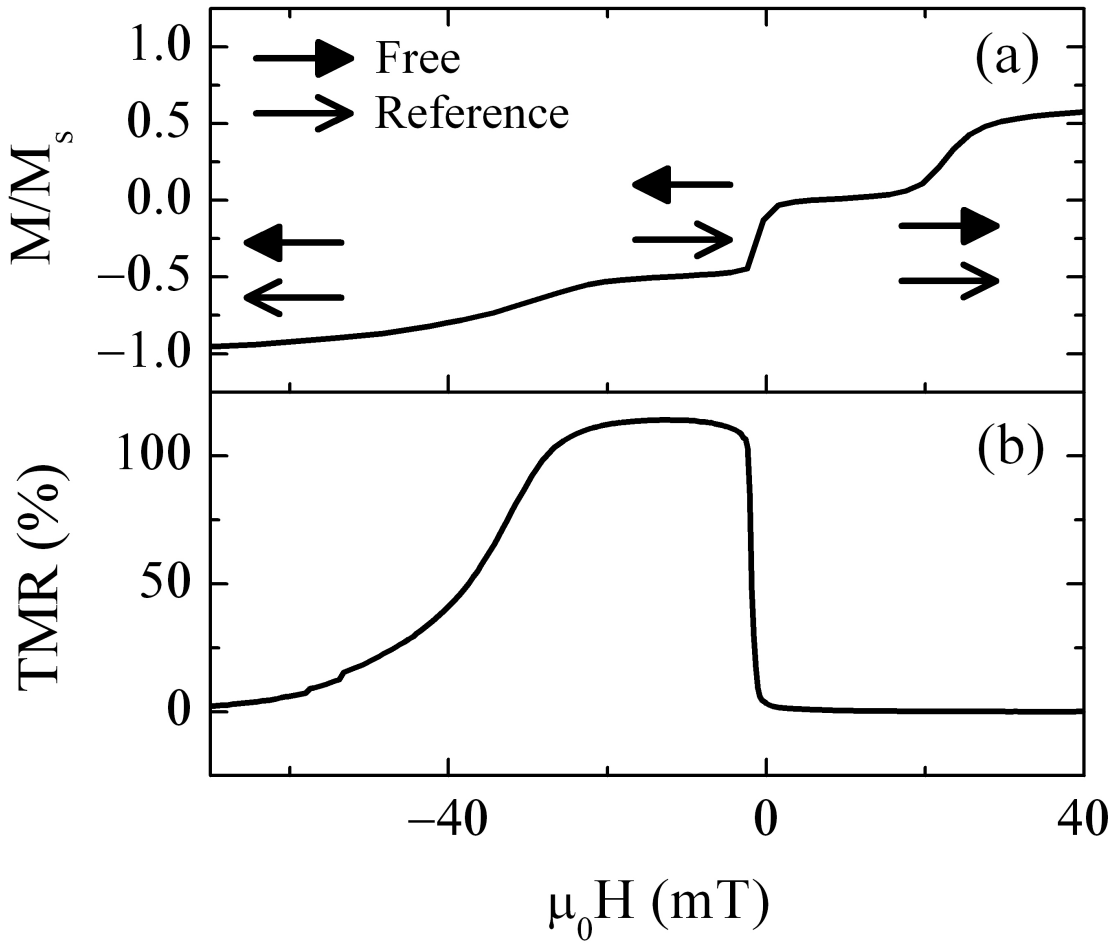

Figure 1

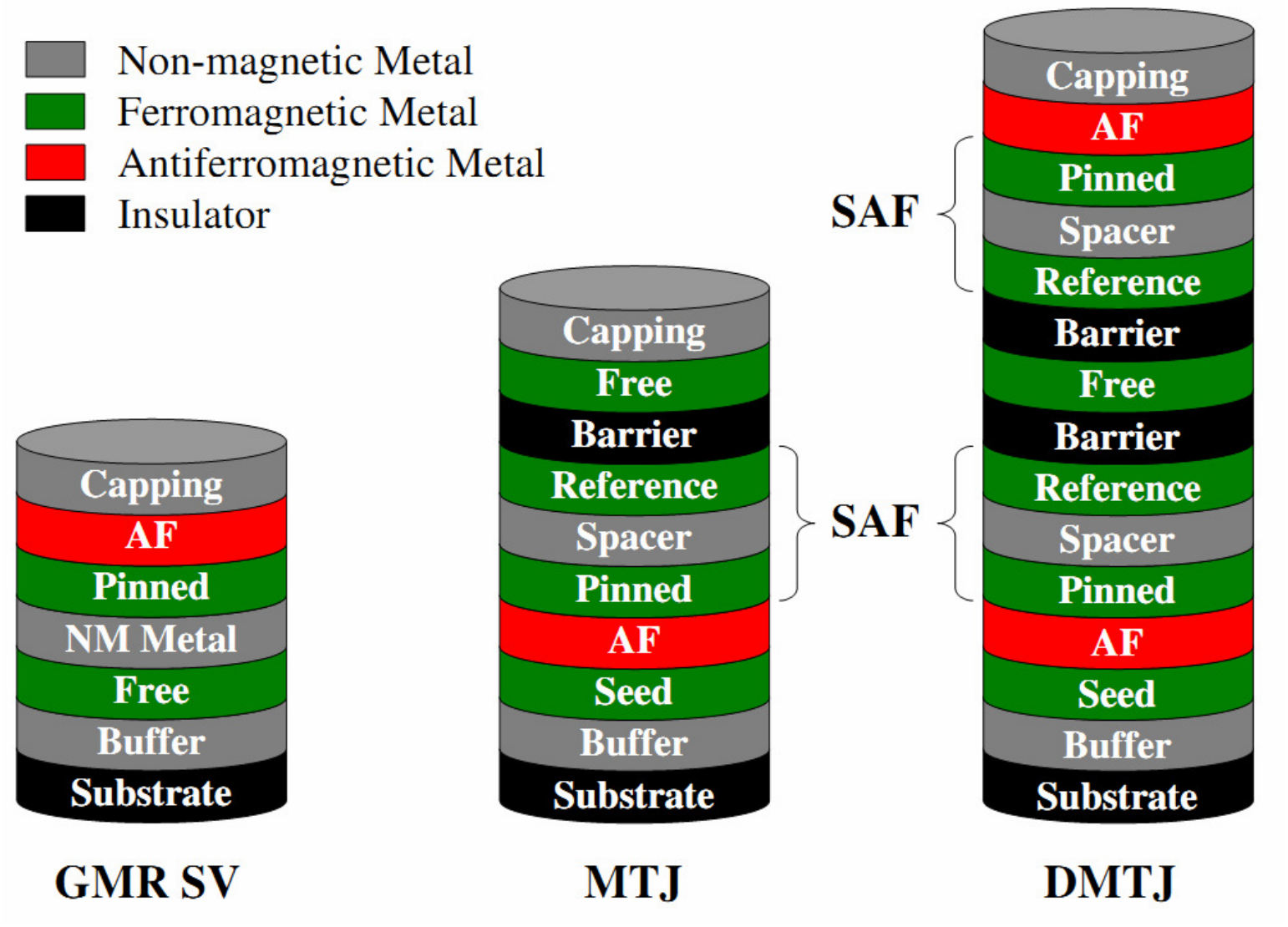
Non-magnetic Metal
Ferromagnetic Metal
Antiferromagnetic Metal
Insulator
Capping
AF
Pinned
NM Metal
Free
Buffer
Substrate
GMR SV
Capping
Free
Barrier
Reference
Spacer
Pinned
AF
Seed
Buffer
Substrate
SAF
MTJ
Capping
AF
Pinned
Spacer
Reference
Barrier
Free
Barrier
Reference
Spacer
Pinned
AF
Seed
Buffer
Substrate
SAF
SAF
DMTJ

Figure 2

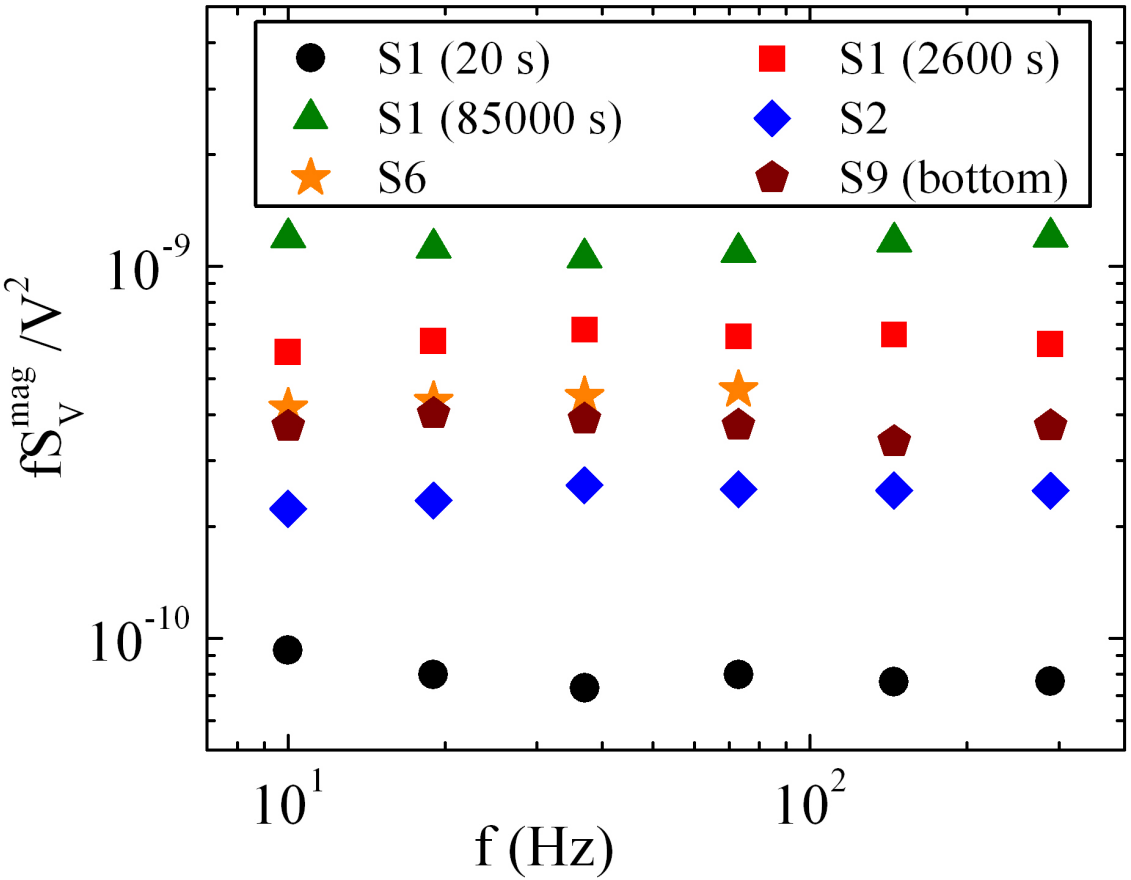
S1 (20 s)
S1 (2600 s)
S1 (85000 s)
S2
S6
S9 (bottom)
10^{-9}
10^{-10}
fS_V^{mag}/V^2
10^1
10^2
f (Hz)

Figure 3

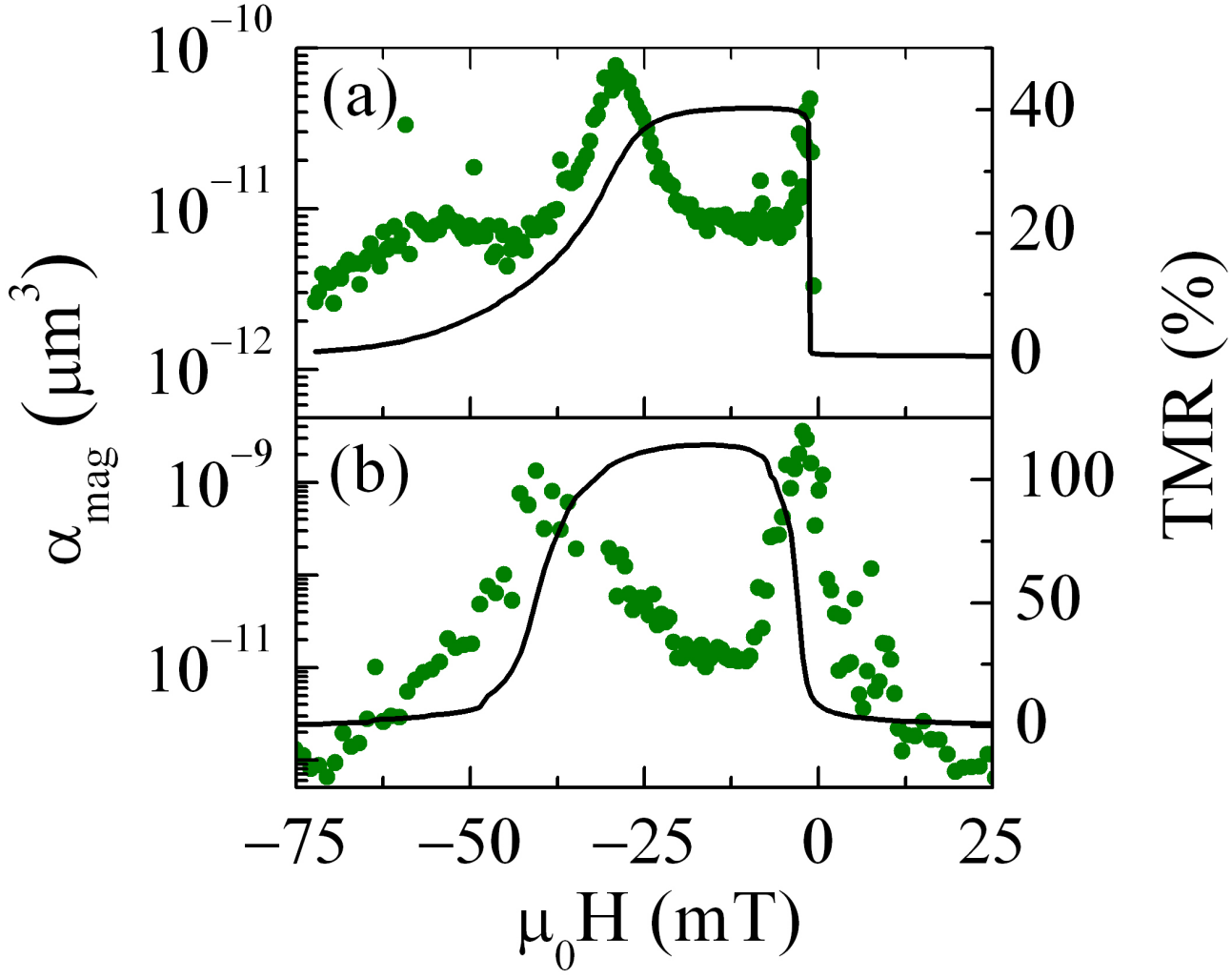
(a)
(b)
10^{-10}
10^{-11}
10^{-12}
10^{-9}
10^{-11}
α_{mag} (μm^3)
40
20
0
100
50
0
TMR (%)
−75
−50
−25
0
25
$\mu_0 H$ (mT)

Figure 4

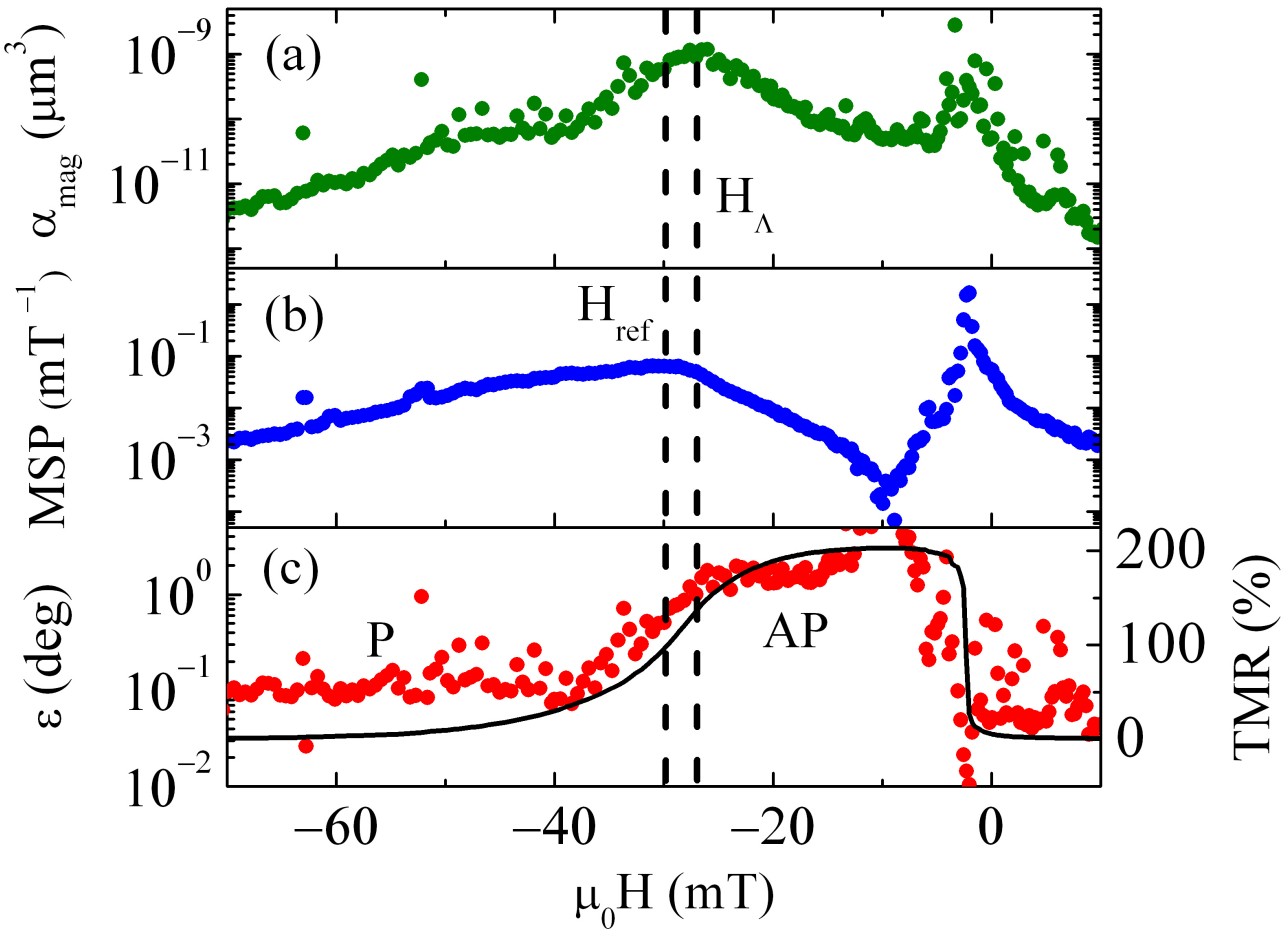
(a)
(b)
(c)
H_Λ
H_{ref}
P
AP
α_{mag} (μm^3)
MSP (mT^{-1})
ε (deg)
TMR (%)
$\mu_0 H$ (mT)
10^{-9}
10^{-11}
10^{-1}
10^{-3}
10^{0}
10^{-1}
10^{-2}
200
100
0
−60
−40
−20
0

Figure 5

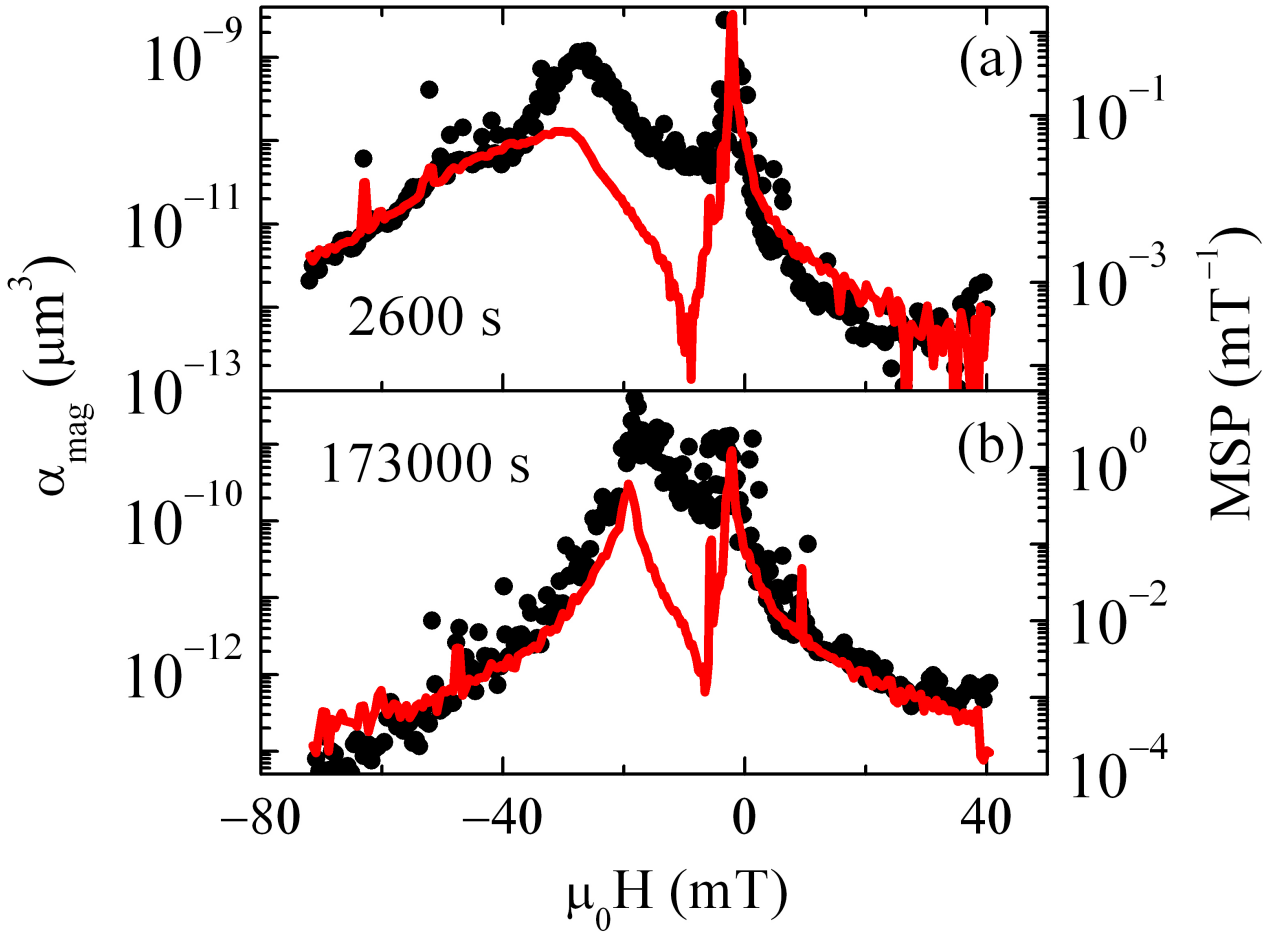
(a)
2600 s
(b)
173000 s
10^{-9}
10^{-11}
10^{-13}
10^{-10}
10^{-12}
10^{-1}
10^{-3}
10^{0}
10^{-2}
10^{-4}
α_{mag} (μm^3)
MSP (mT^{-1})
−80
−40
0
40
$\mu_0 H$ (mT)

Figure 6

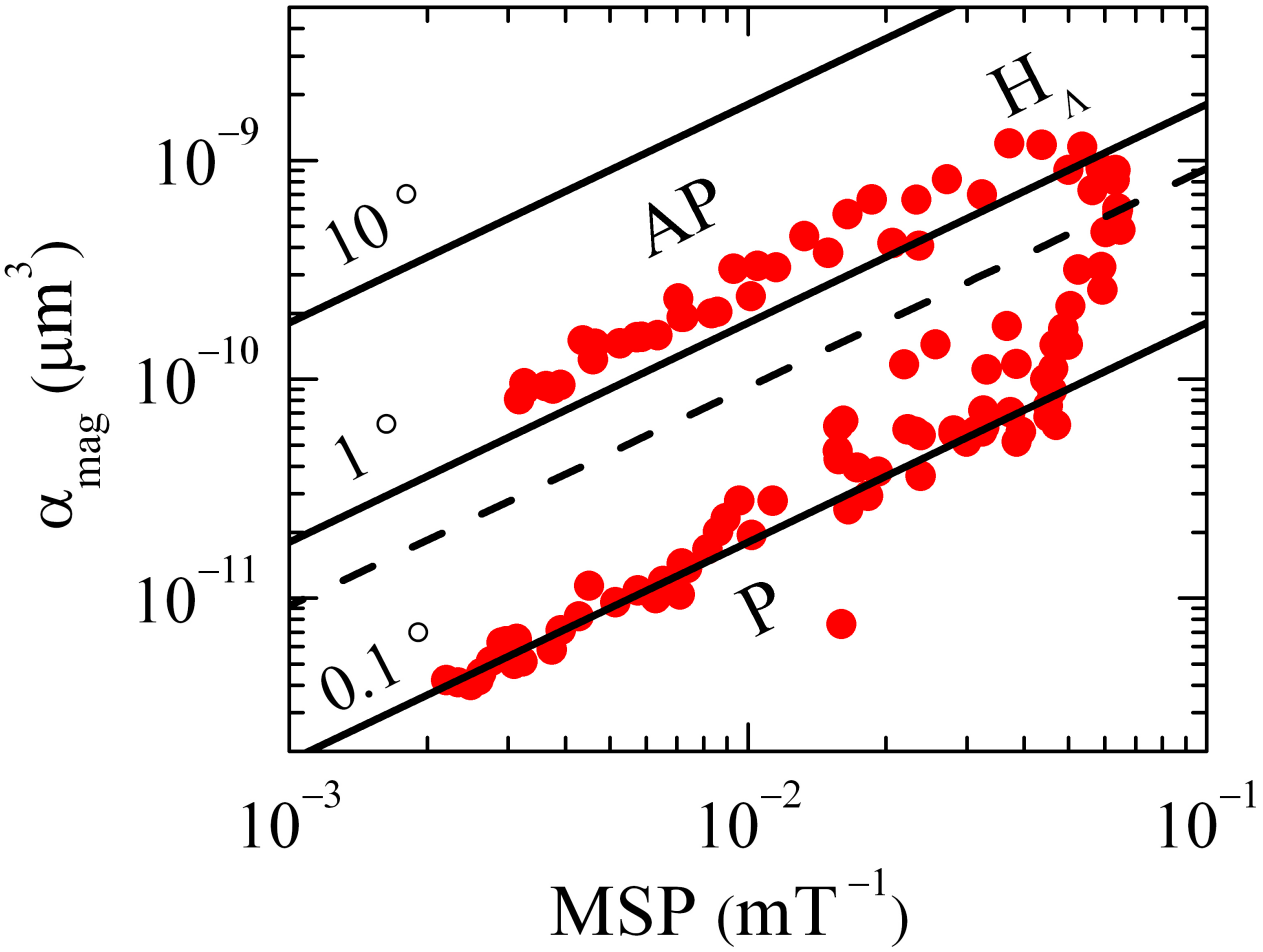
10^{-9}
10^{-10}
10^{-11}
α_{mag} (μm^3)
10°
1°
0.1°
AP
P
H_Λ
10^{-3}
10^{-2}
10^{-1}
MSP (mT^{-1})

Figure 7

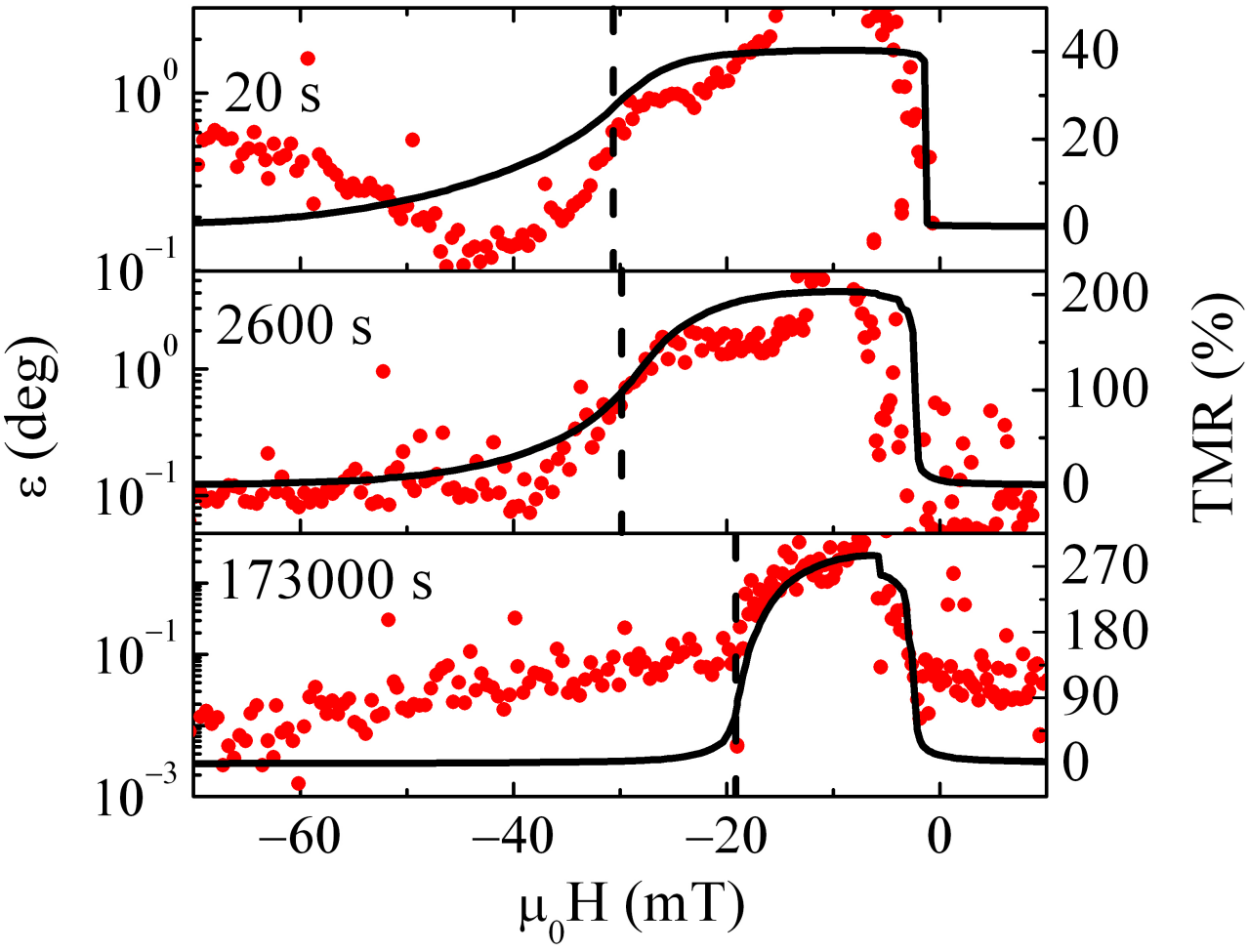
20 s
2600 s
173000 s
ε (deg)
TMR (%)
μ0H (mT)
10^0
10^−1
10^−3
40
20
0
200
100
0
270
180
90
0
−60
−40
−20
0

Figure 8

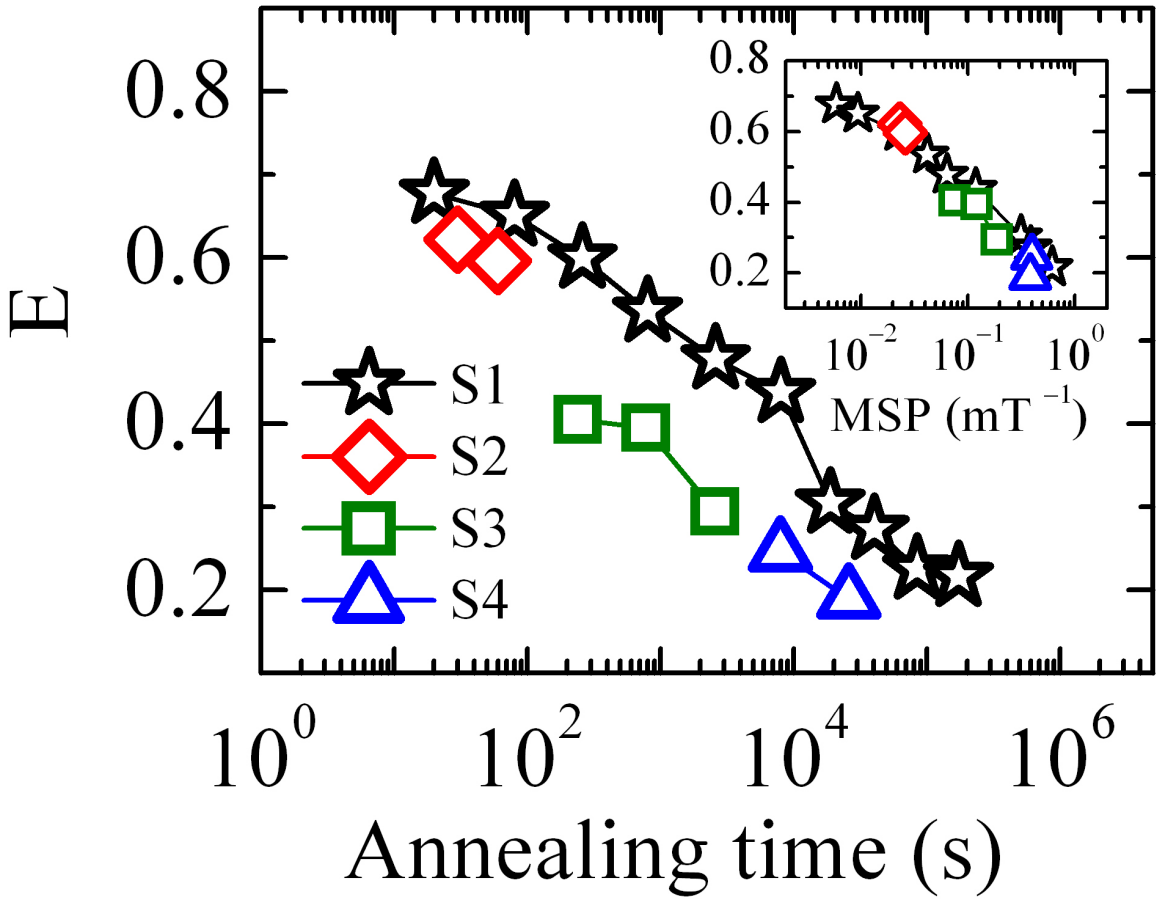
E
0.8
0.6
0.4
0.2
10^0
10^2
10^4
10^6
Annealing time (s)
S1
S2
S3
S4
0.8
0.6
0.4
0.2
10^{-2}
10^{-1}
10^0
MSP (mT^{-1})

Figure 9

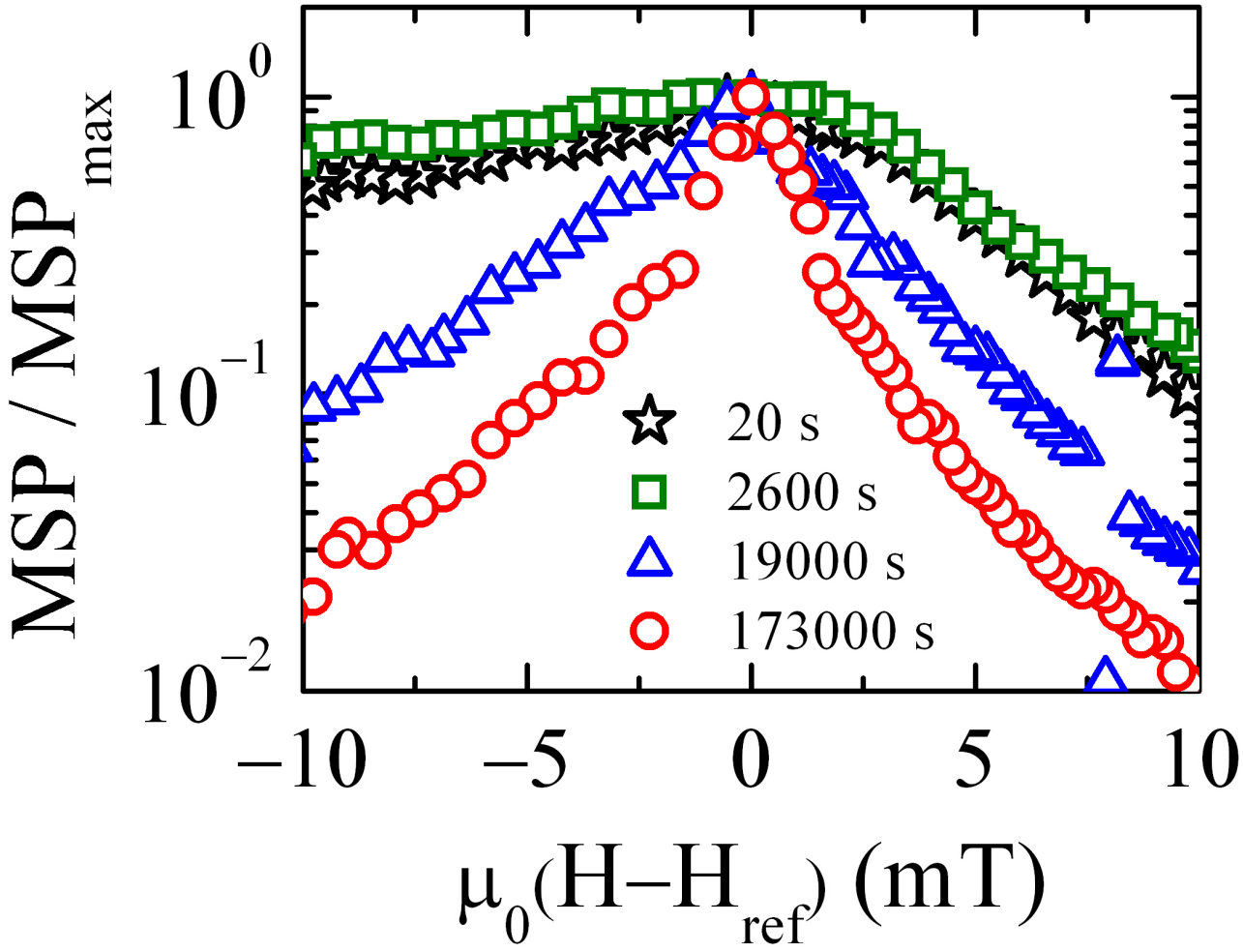
MSP / MSP max
10^0
10^−1
10^−2
−10
−5
0
5
10
μ0(H–Href) (mT)
20 s
2600 s
19000 s
173000 s

Figure 10

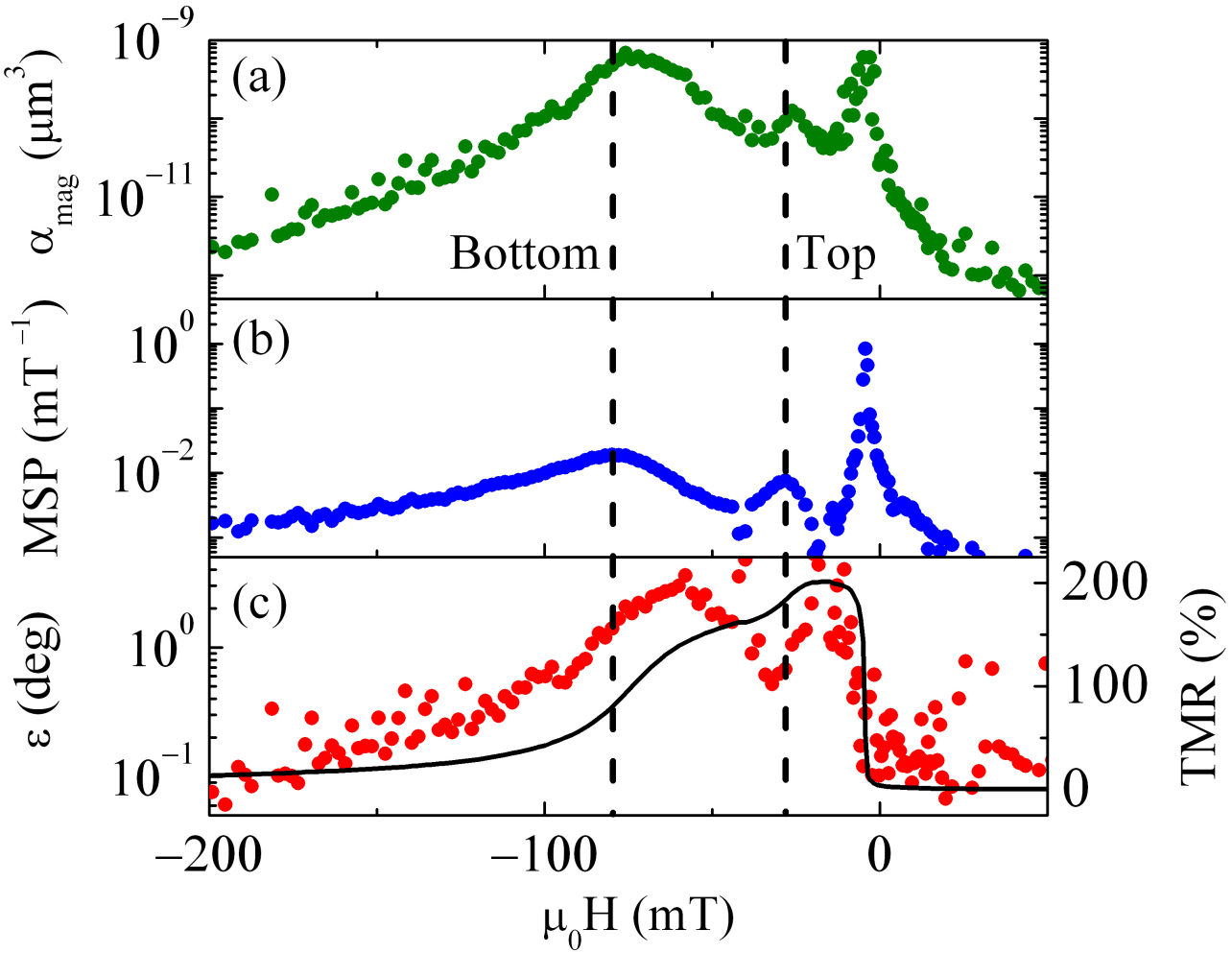
(a)
(b)
(c)
Bottom
Top
10^{-9}
10^{-11}
α_{mag} (μm^3)
10^{0}
10^{-2}
MSP (mT^{-1})
10^{0}
10^{-1}
ε (deg)
200
100
0
TMR (%)
−200
−100
0
$\mu_0 H$ (mT)

Figure 11

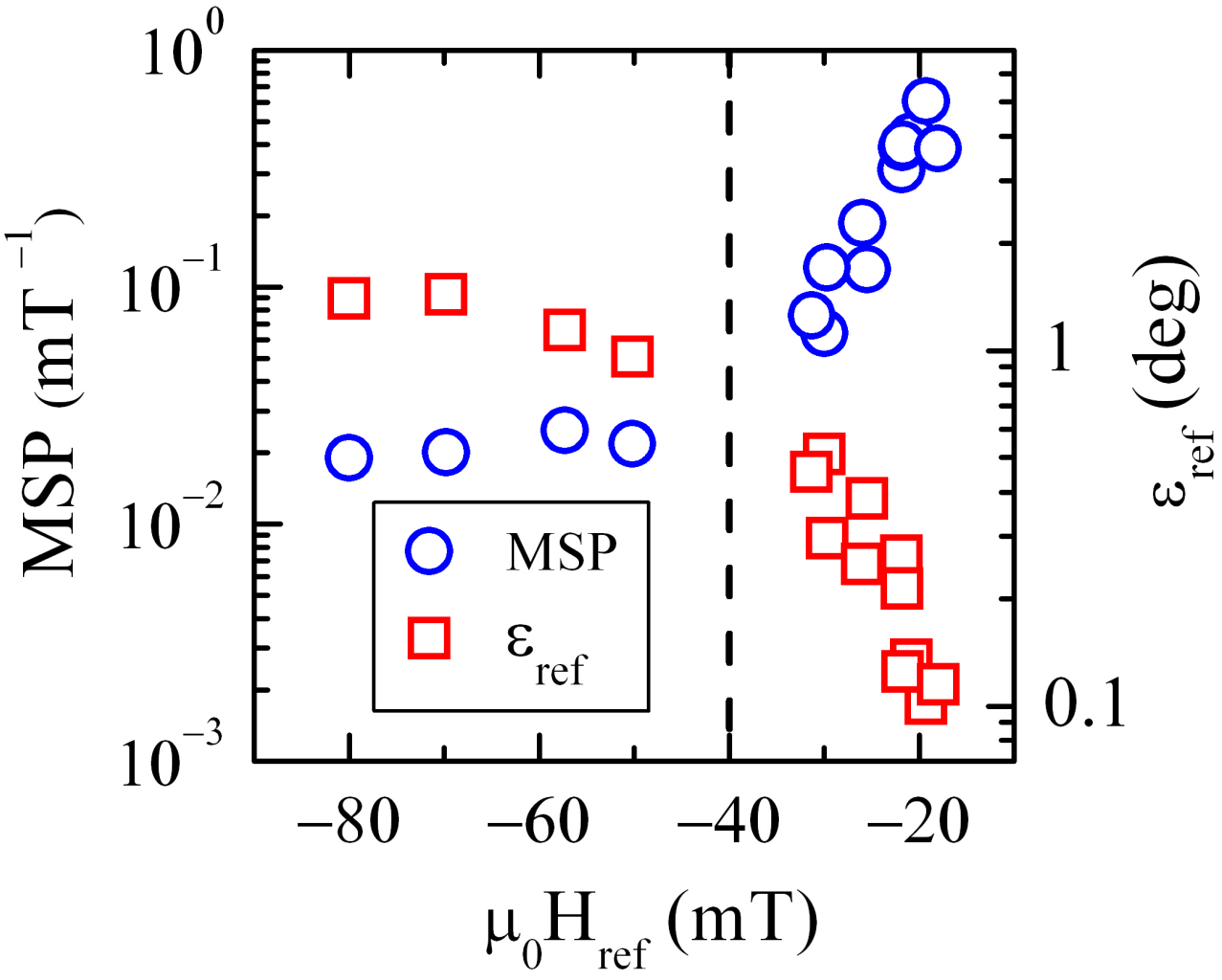
10^0
10^{-1}
10^{-2}
10^{-3}
MSP (mT^{-1})
MSP
ε_{ref}
1
0.1
ε_{ref} (deg)
−80
−60
−40
−20
$\mu_0 H_{ref}$ (mT)

Figure 12

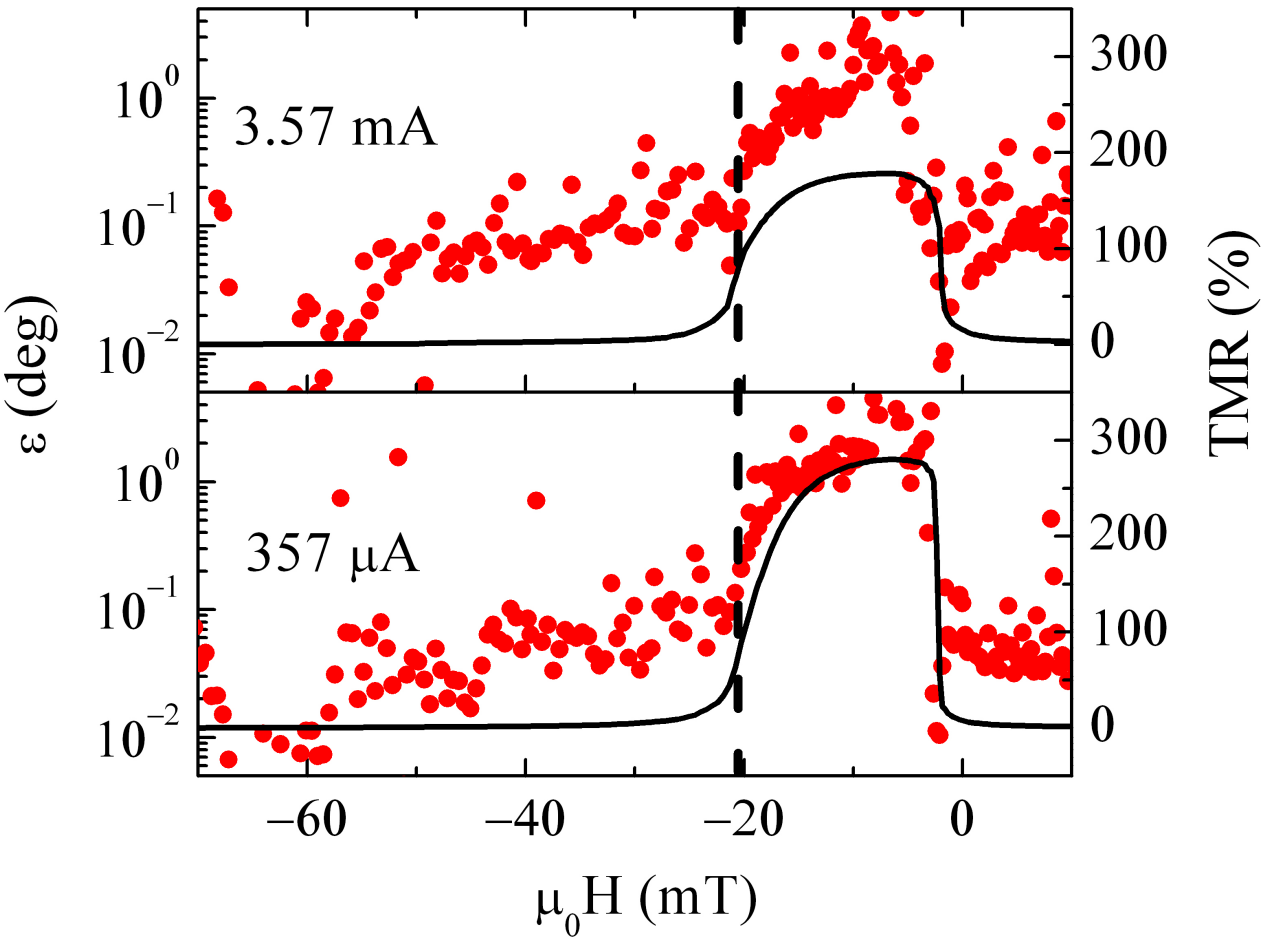

Figure 13

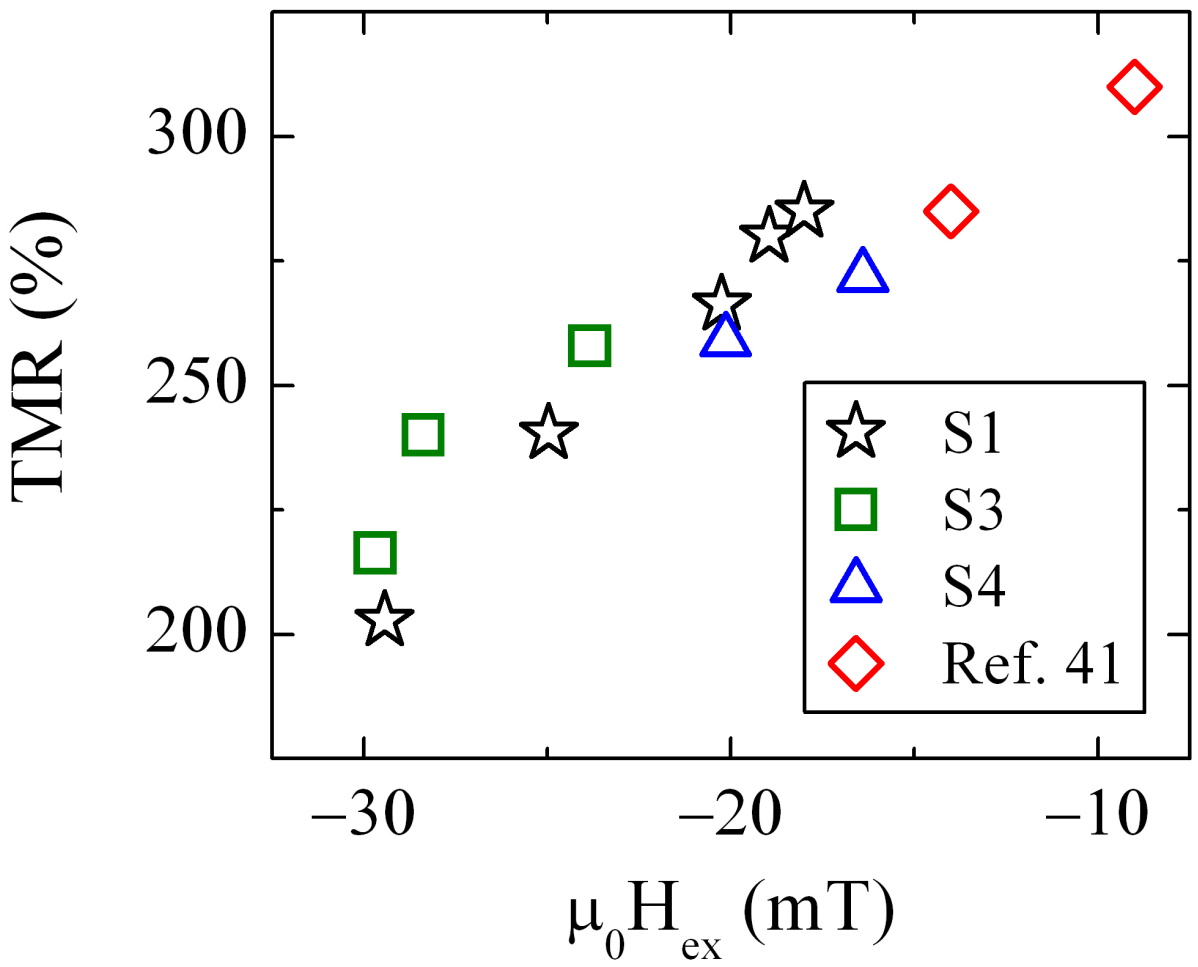

Figure 14